Title: Diet-induced macrophage-driven inflammation fuels pancreatic plasticity and aggressiveness

Ana Galván-del-Rey[1*], Juan Carlos López-Gil[1*], Livia Archibugi[2], Sonia Alcalá[3,4], Julie Earl[4], Michele Bevere[5], Antonio Agostini[6], Aleix Noguera[7,8], Beatriz Parejo-Alonso[9], Alba Royo-García[9], Kyra Fraser[10], Pian Sun[1], Elena Zamorano-Dominguez[1,8], Blanca Rosas-Perez[1], Rebeca Barrero[1], Silvia Jiménez-Parrado[1], Stephen P. Pereira[10], Pilar Acedo[10], Carmine Carbone[6], Claudio Luchini[5], Patricia Sancho[9], Manel Esteller[8,11,12,13], Gabriele Capurso[2,14], Bruno Sainz, Jr.[3,4], Mariano Barbacid[1,8,15] and Carmen Guerra[1,8,15].

Affiliations:

1 Experimental Oncology group, Tumor Biology Programme, Spanish National Cancer Research Center (CNIO), Madrid, Spain.

2 Pancreato-Biliary Endoscopy and Endosonography Division, Pancreas Translational and Clinical Research Center, IRCCS Ospedale San Raffaele, Milan, Italy.

3 Cancer Stem Cells and Fibroinflammatory Microenvironment group, Cancer department, Biomedical Research Institute (IIBm) Sols-Morreale (IIBM) CSIC-UAM, Madrid, Spain.

4 Biomarkers and personalized approach to cancer group (BIOPAC), Area 3-Cáncer, Instituto Ramón y Cajal de Investigación Sanitaria (IRYCIS), Madrid, Spain.

5 ARC-Net Research Centre, University of Verona, Verona, Italy and Department of Diagnostics and Public Health, Section of Pathology, University of Verona, Verona, Italy.

6 Department of Medical and Surgical Sciences, Fondazione Policlinico Universitario "Agostino Gemelli" IRCCS, Rome, Italy.

7 Cancer Epigenetics Group, Josep Carreras Leukaemia Research Institute (IJC), Badalona, Barcelona, Catalonia, Spain.

8 Área Cáncer, Centro de Investigación Biomédica en Red (CIBERONC), ISCIII, Madrid, Spain.

9 Instituto de Investigación Sanitaria Aragón (IIS Aragón), Zaragoza, Spain.

10 Institute for Liver and Digestive Health, Royal Free Hospital Campus, University College London (UCL), NW3 2QG, London, United Kingdom.

11 Cancer Epigenetics Group, Sant Pau Research Institute (IRSantPau), Barcelona, Catalonia, Spain.

12 Institucio Catalana de Recerca i Estudis Avançats (ICREA), Barcelona, Catalonia, Spain.

13 Physiological Sciences Department, School of Medicine and Health Sciences, University of Barcelona (UB), Barcelona, Catalonia, Spain.

14 Vita-Salute San Raffaele University, Milan, Italy.

15 Corresponding authors

** These authors contributed equally.*

Abstract

High-fat diet (HFD) and obesity are increasingly recognized as risk factors of pancreatic ductal adenocarcinoma (PDAC), yet the mechanisms by which dietary fat contribute to oncogenic transformation remain elusive. Using an inducible acinar-specific *Kras*^{G12V}/*Trp53*-loss genetically-engineered mouse model of PDAC, we established early- and late-onset protocols to assess age-dependent susceptibility to HFD. Specifically, HFD accelerated tumorigenesis with poorer prognosis in early-onset mice and, strikingly, enabled full PDAC development in late-onset adult mice otherwise resistant to oncogenic transformation. Tumors arising under HFD activated a distinct transcriptional and epigenetic state enriched in pathways or genes related to stemness, plasticity, and metastatic competence, which was maintained even in tumor-derived cell lines. Mechanistically, fatty acid-educated macrophages secreted the cathelicidin antimicrobial peptide (CAMP), activating P2X purinoceptor 7 (P2RX7) signaling in tumor cells to drive a highly plastic, immune-evasive phenotype reinforced by the expression of the peptidoglycan recognition protein 1 (PGLYRP1), further shielding tumor cells from macrophage phagocytosis. Functionally, HFD-induced tumors displayed enhanced metastatic potential independent of host context. Analysis of 164 human PDAC samples revealed that elevated body-mass index (BMI) was associated to a conserved CAMP-P2RX7-CXCR4 signature, maintained despite weight loss during disease progression. Together, these findings uncover a diet-imprinted macrophage-tumor cell circuit that promotes transformation and accelerates PDAC progression, positioning it as a therapeutic vulnerability in obesity-associated pancreatic cancer.

63 **Introduction**

64 High-fat diet (HFD) consumption and obesity are well-established risk factors for pancreatic ductal
65 adenocarcinoma (PDAC) (1). As processed food intake has dramatically increased worldwide over
66 the past decades in parallel with PDAC incidence, this association gains particular relevance in the
67 context of a disease with a dismal 5-year survival rate of approximately 13% in the US (2). Beyond
68 general PDAC cases, the rising incidence of “early-onset” patients (diagnosed before the age of 50)
69 underscores the contribution of exposome-related factors to disease initiation in younger populations
70 (3). However, traditional endogenous mouse models of PDAC, although invaluable over the past 20
71 years, are limited by the presence of oncogenic driver mutations from embryogenesis. In contrast,
72 patients typically acquire these mutations during adulthood, and many harbor preneoplastic lesions
73 that never progress to PDAC (4). Thus, the role of environmental risk factors and their ability to trigger
74 malignant transformation requires investigation in more biologically relevant models.

75 Our group previously demonstrated that genetically engineered mouse models (GEMMs) harboring
76 *Kras*^{G12V} mutations and *Trp53* loss, a hallmark of advanced PDAC, in the adult pancreas were
77 resistant to oncogenic transformation (5, 6). Only upon induction of chronic pancreatitis with cerulein
78 did mice develop pancreatic intraepithelial neoplasias (PanINs) and PDAC lesions. Acinar cell
79 resistance to transformation appeared reversible once inflammation was established, suggesting that
80 inflammatory events beyond pancreatitis could also drive tumorigenesis. Indeed, *Kras*-mutant acinar
81 cells that escape environmental clearance adopt a stem-like/quiescent state (7), and cancer stem
82 cells (CSCs) expand during the earliest stages of tumor development once inflammation-induced
83 metaplasia arises (8). These findings highlight that inflammatory cues fuel transformed cell plasticity
84 and tumor initiation, yet the impact of dietary habits on this process in adulthood remains poorly
85 defined.

86 Although some studies have shown that HFD accelerates tumorigenesis in embryonic *Kras*-mutated
87 GEMMs (9, 10), mechanistic insights into how diet promotes PDAC progression and metastasis in
88 adult models remain scarce. In this work, we evaluated the transformation capacity of adult acinar
89 cells upon *Kras*^{G12V} activation and *Trp53* loss using an inducible GEMM for PDAC that enables

90 temporal control of oncogenic expression, allowing direct comparison between early- and late-onset
91 protocols. We found that HFD induces systemic inflammation that drives PanINs and PDAC formation.
92 Notably, HFD-induced tumors exhibited a distinct transcriptomic program associated with enhanced
93 plasticity and metastatic potential. Mechanistically, fatty acid-exposed macrophages promoted
94 inflammatory signaling through the cathelicidin antimicrobial peptide (CAMP)-P2X purinoceptor 7
95 (P2RX7) axis, ultimately inducing this phenotype in tumor cells and revealing a potential therapeutic
96 opportunity to target HFD-driven PDAC.

97 **Results**

98 **HFD promotes pancreatic tumorigenic transformation in an early adulthood onset model of**
99 **PDAC.** To study the contribution of high-fat diet in pancreatic tumorigenesis we took advantage of an
100 inducible GEMM of PDAC with $KRAS^{G12V/+}$ and $P53^{KO}$, which mimics the mutational characteristics of
101 advanced PDAC (*Elas*-tTA/*tetO*-Cre; $Kras^{LSLG12V/+}$; $Trp53^{lox/lox}$). We developed two risk factors
102 exposure protocols to model the early and late onset development of the disease, in addition to the
103 classical embryonic setting as a reference. For the early onset (P21), we maintained mice on
104 doxycycline (DOX) for three weeks and then DOX was removed and exposure to high-fat diet (HFD)
105 was initiated. As DOX requires approximately one month for complete clearance, HFD exposure prior
106 to full induction of the mutations repressed by DOX resembles adolescents with HFD-like habits
107 before mutation acquisition (**Figure 1A**). Mice were kept on HFD until one year of age or humane
108 endpoint. For the embryonic setting, *Elas*-tTA/*tetO*-Cre; $Kras^{LSLG12V/+}$; $Trp53^{lox/lox}$ mice were kept
109 without DOX allowing for transgenes recombination during embryonic development leading to 100%
110 disease development. As expected, both female and male mice gained weight after HFD-exposure
111 (**Figure S1A**) and the expected systemic effects caused by the diet were assessed, including fatty
112 liver (**Figure S1B**), acinar-to-adipose replacement in the pancreas, intra-acinar lipid droplets
113 accumulation (**Figure S1C**), and brown to white adipose tissue transformation (**Figure S1D**). We
114 further confirmed that HFD exposure alone does not lead to preneoplastic lesions (PanINs) formation
115 in wild-type (WT) mice, demonstrating that the diet by itself does not trigger neoplastic transformation
116 (**Figure S1E**).

117 As reported in previous studies from the laboratory, adult acinar cells present an oncogenic
118 transformation resistance that increases with age, with no tumor formation when mutations are
119 induced at 60 days post-birth (5, 6) (**Figure 1B**). Interestingly, P21 mice exhibited an intermediate
120 phenotype, showing preneoplastic lesions and full PDAC, but with an increased resistance to tumor
121 development compared with the embryonic model (**Figure 1B**). Notably, P21 mice exposed to HFD
122 developed tumors earlier than P21 control mice, although later than the embryonic model (**Figure 1C-**
123 **D**). Despite these differences, survival was comparable between the P21 HFD protocol and the
124 embryonic model, and in both cases significantly shorter than in the P21 control group (**Figure 1D**).
125 Histological analysis of these tumors revealed distinct tumor phenotypes, with control tumors
126 displaying a more differentiated epithelial morphology characterized by ductal-like structures,
127 whereas tumors arising under HFD conditions mainly exhibited a squamous/mesenchymal-like
128 phenotype (**Figure 1E**). These results suggest that HFD promotes early onset of PDAC tumors,
129 affecting survival in an early adulthood context.

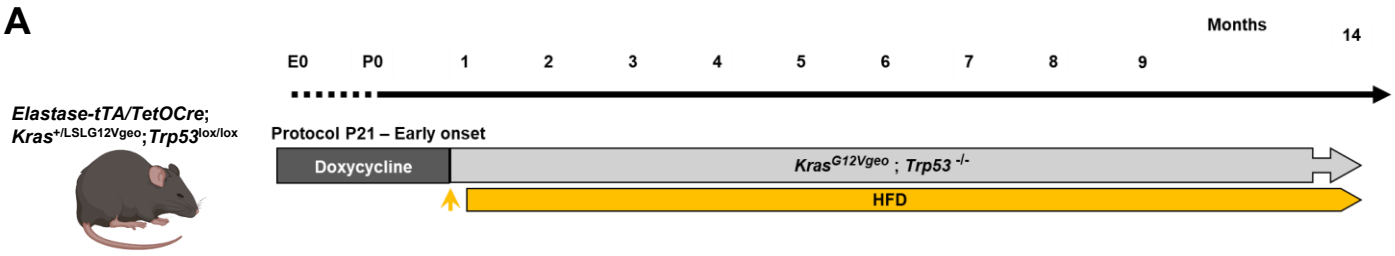
A
Months
14
E0
P0
1
2
3
4
5
6
7
8
9
Elastase-tTA/TetOCre;
Kras+/LSLG12Vgeo;Trp53lox/lox
Protocol P21 – Early onset
Doxycycline
KrasG12Vgeo ; Trp53 -/-
HFD

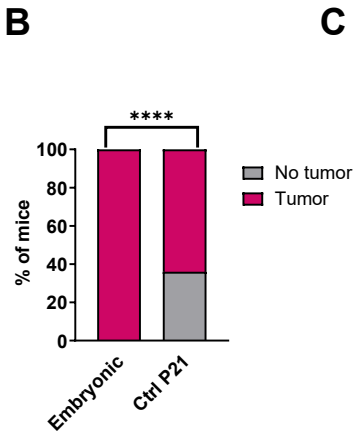
B
****
% of mice
100
80
60
40
20
0
No tumor
Tumor
Embryonic
Ctrl P21

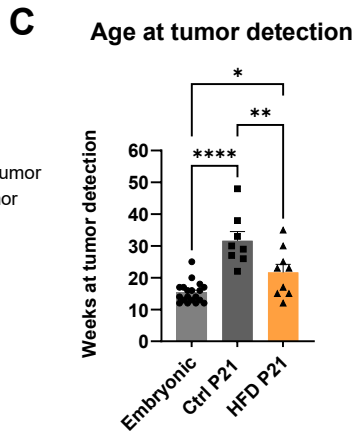
C
Age at tumor detection
Weeks at tumor detection
60
50
40
30
20
10
0
*
**
****
Embryonic
Ctrl P21
HFD P21

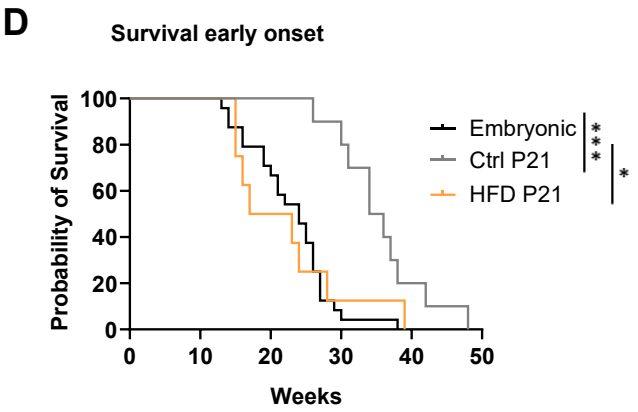
D
Survival early onset
Probability of Survival
100
80
60
40
20
0
0
10
20
30
40
50
Weeks
Embryonic
Ctrl P21
HFD P21
***
*

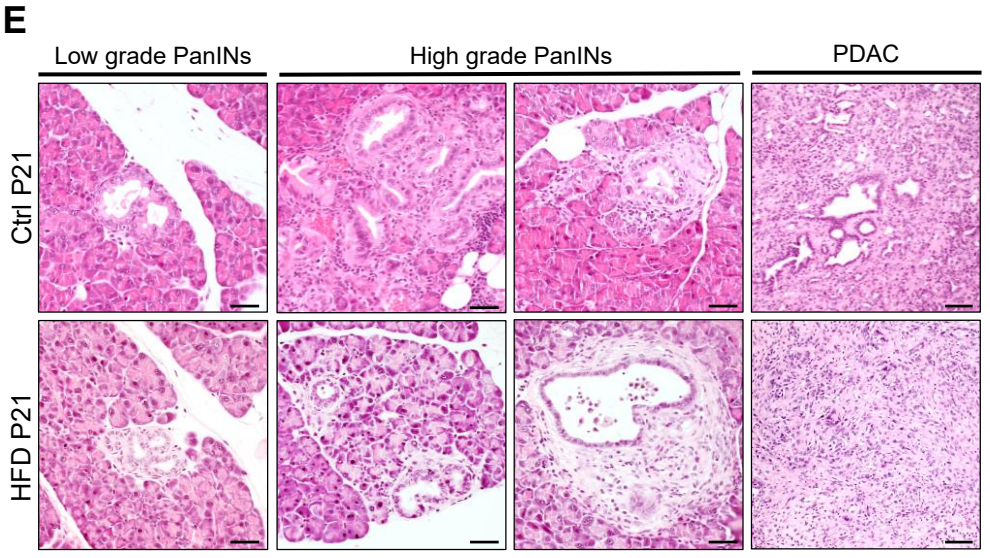
E
Low grade PanINs
High grade PanINs
PDAC
Ctrl P21
HFD P21

138 ***Figure 1. High-fat diet promotes tumorigenesis in early-onset adult PDAC mouse models**. **A)***
139 *Representative scheme of the protocol employed to study the effect of high-fat diet (HFD) in early onset*
140 *pancreatic cancer (P21).* ***B)*** *Percentage of mice from the embryonic and P21 arms in which tumors were*
141 *detected (embryonic n=19, controls (Ctrl) P21 n=14). P values as determined by Chi-square test and Fisher´s*
142 *exact test.* ***C)*** *Histogram showing the weeks at tumor detection for the embryonic, Ctrl and HFD-exposed mice*
143 *from the P21 protocol. Shown is the mean ± SEM (embryonic n=19, Ctrl P21 n=8, HFD n=9; P values as*
144 *determined by One-way ANOVA, Tukey test).* ***D)*** *Kaplan-Meier plot showing the overall survival of mice from*
145 *the embryonic and P21 (both Ctrl and HFD) settings (embryonic n=24, Ctrl P21 n=10, HFD n=8, P values as*
146 *determined by Mantel-Cox test).* ***E)*** *Representative brightfield microscopy images of hematoxylin and eosin-*
147 *stained pancreata at different stages of tumor development in the P21 fed with Ctrl diet (top panel) or HFD*
148 *(bottom panel). Scale bar= 50 µm. P values: *, <0.05; **, <0.01; ***, <0.001; ****, <0.0001.*

149

150 **HFD-promoted pancreatic tumors displayed a mesenchymal-like phenotype.** Based on the
151 histological differences observed before, we conducted a marker-based characterization of the P21
152 control and HFD-promoted tumors. We found that control tumors displayed high levels of cytokeratin
153 19, a common marker of epithelial tumors, while HFD-promoted tumors expressed markedly lower
154 levels (**Figure 2A**). On the other hand, vimentin, a marker of mesenchymal tumors, was
155 overexpressed in HFD tumor cells, while in control tumors it was mainly restricted to fibroblasts
156 (**Figure 2A**). Consistently, the epithelial marker EpCAM, was also highly reduced in HFD-promoted
157 tumors (**Figure 2B-C**). Interestingly, in the HFD-promoted tumors we observed a population of cells
158 that expressed both EpCAM and vimentin, suggesting that HFD could induce a hybrid
159 epithelial/mesenchymal phenotype (**Figure 2B-C**).

160 To better understand the molecular changes produced by HFD in tumor cells, we derived primary cell
161 cultures from both P21 control and HFD-induced tumors. As expected, and consistent with the
162 phenotype observed *in vivo*, control cell lines exhibited an epithelial morphology in culture, whereas
163 HFD-induced (iHFD) tumor cell lines displayed a mesenchymal morphology (**Figure 2D**). In line with
164 this, iHFD cell lines showed a reduction of *Krt19, Cdh1 and Gata6*, genes associated with an
165 epithelial/classical-like phenotype. Likewise, we found an upregulation of *Gata2*¸ which regulates
166 *Gata6* expression in an opposite manner (11, 12). Unexpectedly, we observed a decrease in *Cdh2*
167 and an increase in *Tff2,* mesenchymal and epithelial-associated markers respectively (**Figure 2E**).
168 These results indicated that HFD induced a hybrid phenotype between classical/epithelial and
169 basal/mesenchymal states and suggested that HFD promotes a plastic state in tumor cells.

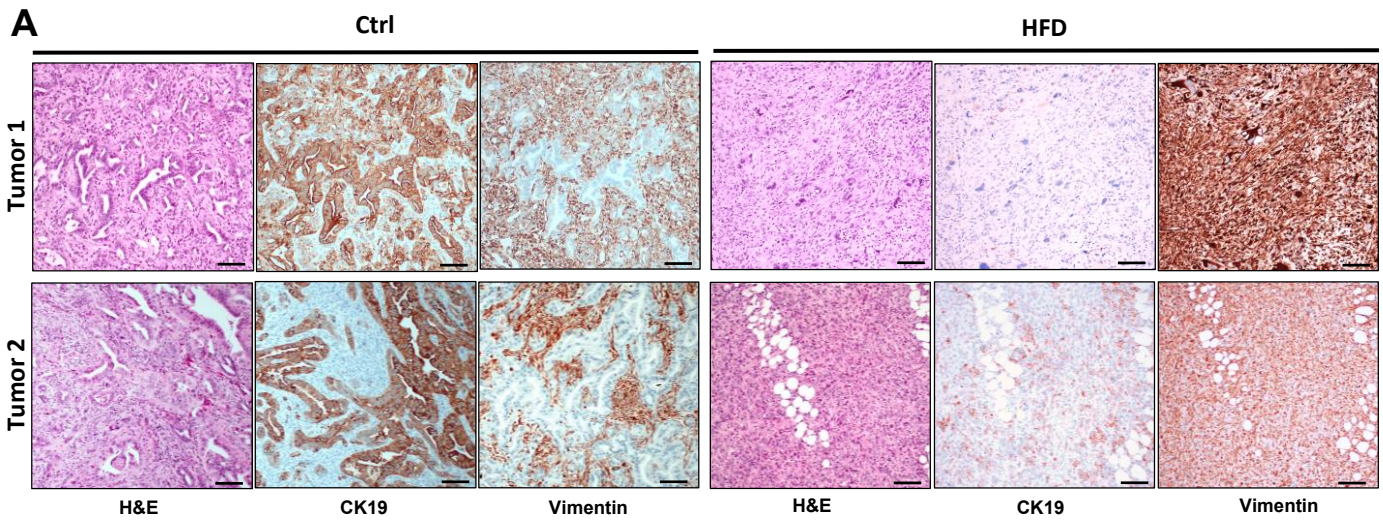
A
Ctrl
HFD
Tumor 1
Tumor 2
H&E
CK19
Vimentin
H&E
CK19
Vimentin

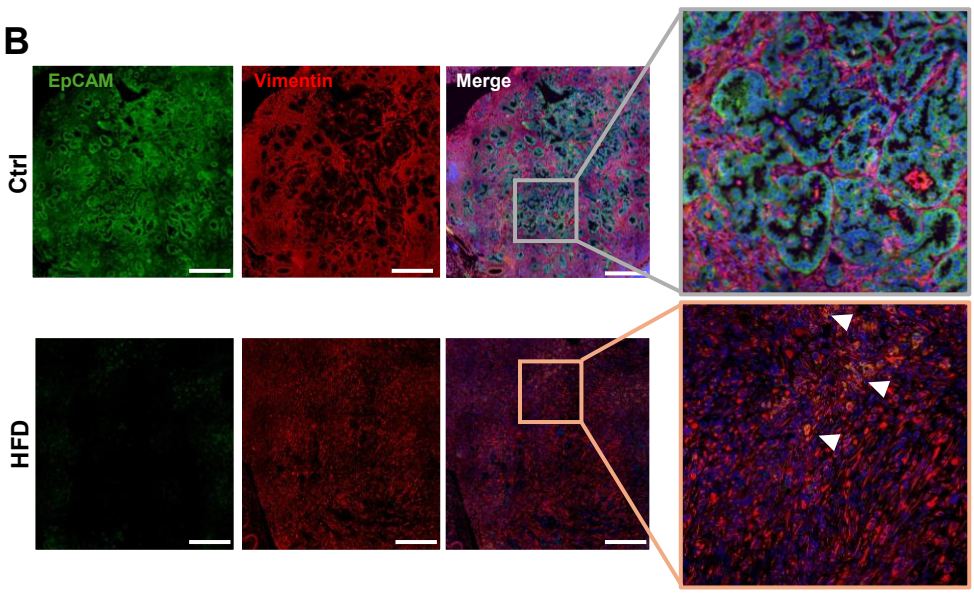
B
EpCAM
Vimentin
Merge
Ctrl
HFD

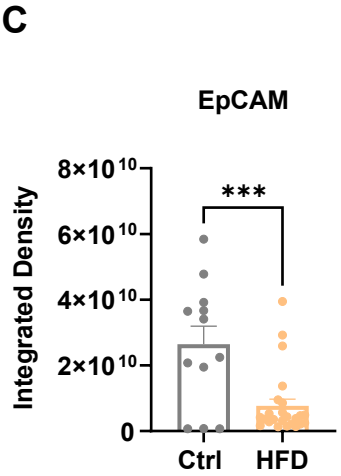
C
EpCAM
Integrated Density
8×10 10
6×10 10
4×10 10
2×10 10
0
***
Ctrl
HFD

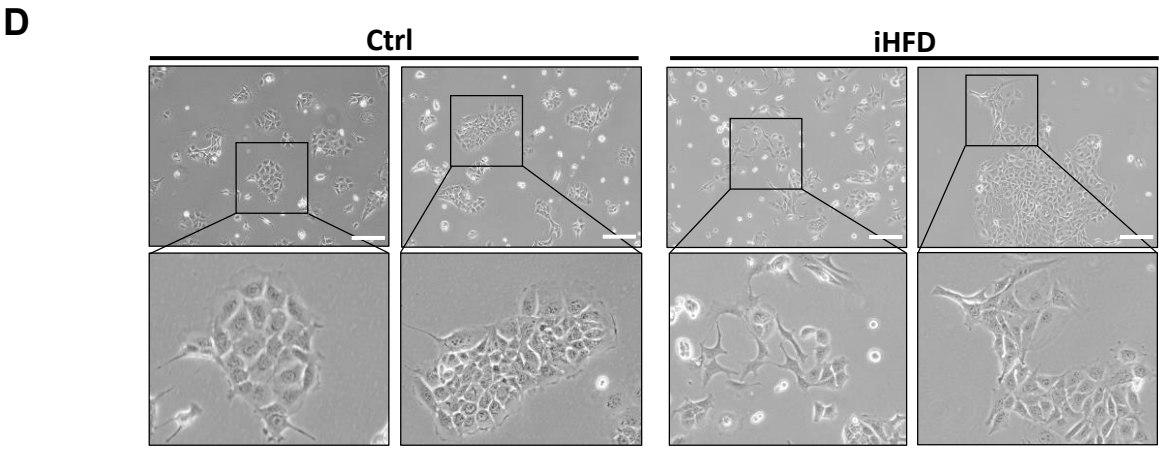
D
Ctrl
iHFD

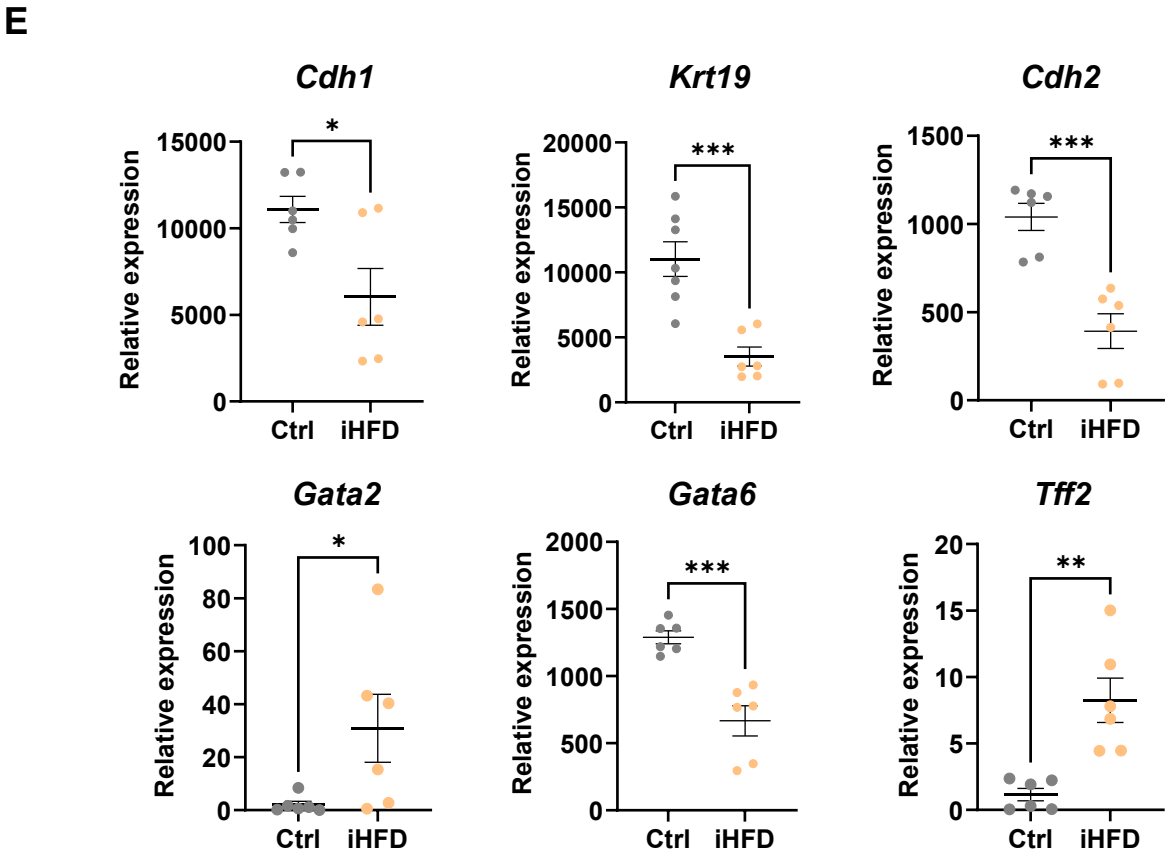
E
Cdh1
Krt19
Cdh2
Gata2
Gata6
Tff2
Relative expression
Ctrl
iHFD
*
***
**

171 ***Figure 2. Histology and morphological characterization of control and high-fat diet-promoted tumors***
172 ***and primary tumor-derived cells. A)*** *Representative brightfield microscopy images of hematoxylin and eosin*
173 *(H&E), along with cytokeratin 19 (CK19) and vimentin immunohistochemistry from two tumors generated in P21*
174 *control (Ctrl) and HFD-fed mice. Scale bar= 50 µm.* ***B)*** *Representative IF confocal microscopy images from Ctrl*
175 *and HFD tumors stained with EpCAM (green, epithelial tumor cells), Vimentin (red, mesenchymal tumor cells*
176 *and fibroblasts) and DAPI (blue, nuclei). Arrowheads indicate double-positive EpCAM/Vimentin tumor cells.*
177 *Scale bar= 500 µm.* ***C)*** *Quantification of the integrated density for EpCAM staining in Ctrl and HFD tumors.*
178 *Shown is the mean ± SEM for each measured field (n=7 mice, 3 for Ctrl and 4 for HFD; P values as determined*
179 *by unpaired T-test).* ***D)*** *Representative brightfield microscopy images of P21 Ctrl and HFD-induced (iHFD)*
180 *primary tumor-derived cell lines. Scale=50µm.* ***E)*** *Relative expression of mRNA levels measured by RT-qPCR*
181 *of the indicated genes in Ctrl and iHFD primary tumor cell lines. Shown is the mean ± SEM (n=6, P values as*
182 *determined by unpaired T-test). P values: *, <0.05; **, <0.01; ***, <0.001; ****, <0.0001.*

183

184 **HFD induces transcriptomic and epigenetic changes in tumor cell state.** To interrogate in-depth
185 the transcriptional state of iHFD tumor cells, we performed RNA sequencing analysis of six control
186 and six iHFD P21 cell lines. We first found that iHFD cells exhibited higher transcriptomic differences
187 among themselves than control cells (**Figure 3A**). We next performed a differential gene expression
188 analysis, and found significantly upregulated genes associated with extracellular matrix remodelling
189 (i.e., *Fgfr1, Loxl1, Mmp7, Has2*), stemness (i.e., *Prom2, Pglyrp1, Isg15, Agr2, Fn1*), mesenchymal
190 identity and metastatic behaviour (i.e., *Snai1, Zeb2, Grem1, Ngfr, Plau, Foxd1, Foxc1*), and immune
191 evasion (i.e., *Csf1r, Cxcl5, Thbs1, Ccl7, Ccl9, Pglyrp1*) (**Figure 3B**). Among the downregulated genes
192 in iHFD we found mainly genes associated with mitochondria activity (*mt-Co3, mt-Nd3, Ndufb4*). In
193 addition, we found that *Gata2* was upregulated, consistent with the aforementioned data, sustaining
194 the idea of the extinction of the classical subtype programme (**Figure 3B**). To better characterise
195 these transcriptomic changes, we performed Gene Set Enrichment Analysis (GSEA) employing
196 Molecular Signature Database and custom gene sets. Interestingly, we found upregulated a gene
197 signature related to increased tumorigenesis by chemical induction (**Figure 3C)**, as expected from a
198 tumor induced by an external agent such as diet. Apart from this, we found pathways mainly
199 associated to epithelial-to-mesenchymal transition (EMT) and the acquisition of mesenchymal identity
200 and trajectory (13), stemness and plasticity, inflammation and immune system modulation (IL1β and
201 interferon response, and antimicrobial response), ECM organisation (FGF-response and collagen
202 organisation), and, as expected under HFD-induced nutrient overload, nutrient response (**Figure 3C,**
203 **S2A-E**). Based on this, we also compared the expression of marker genes associated with plasticity
204 and stemness in PDAC (8, 14-26), and we found that iHFD cells presented a general increase in the

205 expression of some (but not all) genes including *P2rx7, Pglyrp1, Agr2, Sox9,* and *Ror2* (**Figure 3D**).
206 As this hybrid/plastic phenotype remains stable in the iHFD cell lines, we evaluated epigenomic
207 changes at the DNA methylation level for these cell lines. Interestingly, this analysis suggested that
208 the global methylome clusters the samples per group (**Figure S2F**). We calculated the mean
209 methylation value per CpG sites per group, and the difference among groups. We selected the CpG
210 sites that had an absolute methylation difference higher than 0.33 between groups, and then, we
211 applied a linear regression model, obtaining 2,526 CpG sites differentially methylated (adjusted p-
212 value<0.05). From them, 92.12% (n=2,327) were hypomethylated in iHFD in comparison to the control
213 group (**Figure S2G**), suggesting that HFD likely promotes gene upregulation. Moreover, most of these
214 CpG sites that were differentially methylated were located at the 5' regulatory region of the genes
215 (42.91%; n=1,084) (**Figure S2H**). Then, we used the differentially methylated CpG sites to cluster the
216 samples (**Figure S2I**) and we performed an enrichment analysis with EnrichR using the genes that
217 had at least one CpG site differentially methylated. Using the Panther database, we found 2 pathways
218 differentially regulated, the WNT signaling pathway and the cadherin pathway (**Figure S2J**),
219 supporting that HFD influences the plastic-like EMT state of tumor cells.

220 To cross validate the transcriptomic results with human data, we took advantage of a database
221 including 164 endoscopy-guided ultrasound (EUS) biopsies of PDAC patients of all stages sequenced
222 by bulk RNA-seq (27). First, we divided patients according to their BMI at the time of diagnosis,
223 considering equal to or higher than 25, patients with overweight or obesity; and patients with less than
224 25 as normal weight or lean (**Figure 3E**). When we compared both groups and performed differential
225 gene expression analysis, we found upregulated several genes associated with inflammation (i.e.,
226 *IL1B, TNF, OSM*), antimicrobial response associated with stemness (i.e., *CAMP, PGLYRP1, LTF*),
227 CSCs markers related also to metastases (i.e., *P2RX7, ALK, CXCR4*) and genes involved in immune
228 evasion (*CXCL8, SPP1, S100A9, CD86, CCL7, CCL2*) (**Figure 3F**); some of them also upregulated
229 in our murine dataset. Interestingly, GSEA analysis revealed a significant enrichment in pathways
230 related to macrophages, including those associated with lipids, as well as inflammatory responses
231 mediated by IL1β, TNFα, IL8, or interferons. We also observed enhanced antimicrobial activity via

232 antimicrobial peptides (**Figure 3F, S3A**); as well as several pathways associated with oncogenic
233 KRAS activity, ERK1/2 and MAPK signaling pathways (**Figure S3B**). Likewise, patients with higher
234 BMI presented an enrichment in genes associated with increased blood vessel formation and
235 enhanced migration (**Figure S3C**), as well as response to lipids (**Figure 3G**). Additionally, we
236 generated a gene signature from our murine dataset based on the upregulated genes in iHFD cells
237 (GALVAN_HFD) and assessed its enrichment in the human cohort. As expected, patients with high
238 BMI were significantly enriched for this murine-derived gene signature (**Figure 3G**). Notably, both
239 mouse and human datasets mainly showed downregulation of pathways associated with oxidative
240 phosphorylation (**Figure 3H**). As most of these pathways were common between our human and
241 murine datasets, we compared the genes driving these processes and found 79 commonly
242 upregulated and 36 downregulated (**Figure S4A-B**). Remarkably, we identified P2RX7, an ATP-gated
243 calcium channel and known CSC marker, among the common upregulated genes. P2RX7 is
244 associated to EMT and stemness promotion acting as a receptor for the cathelicidin antimicrobial
245 peptide (*Camp*/CAMP in mice, *CAMP*/hCAP-18/LL-37 in humans), also upregulated in patients with
246 high BMI (**Figure 3F**) (19). These data, along with the enrichment in gene signatures associated to
247 antimicrobial peptides and calcium signaling, led us to hypothesize that HFD could be driving the
248 P2RX7-CAMP axis, promoting a highly plastic, stem-like state in tumor cells driving aggressiveness
249 and tumor progression.

250

251

252

253

254

255

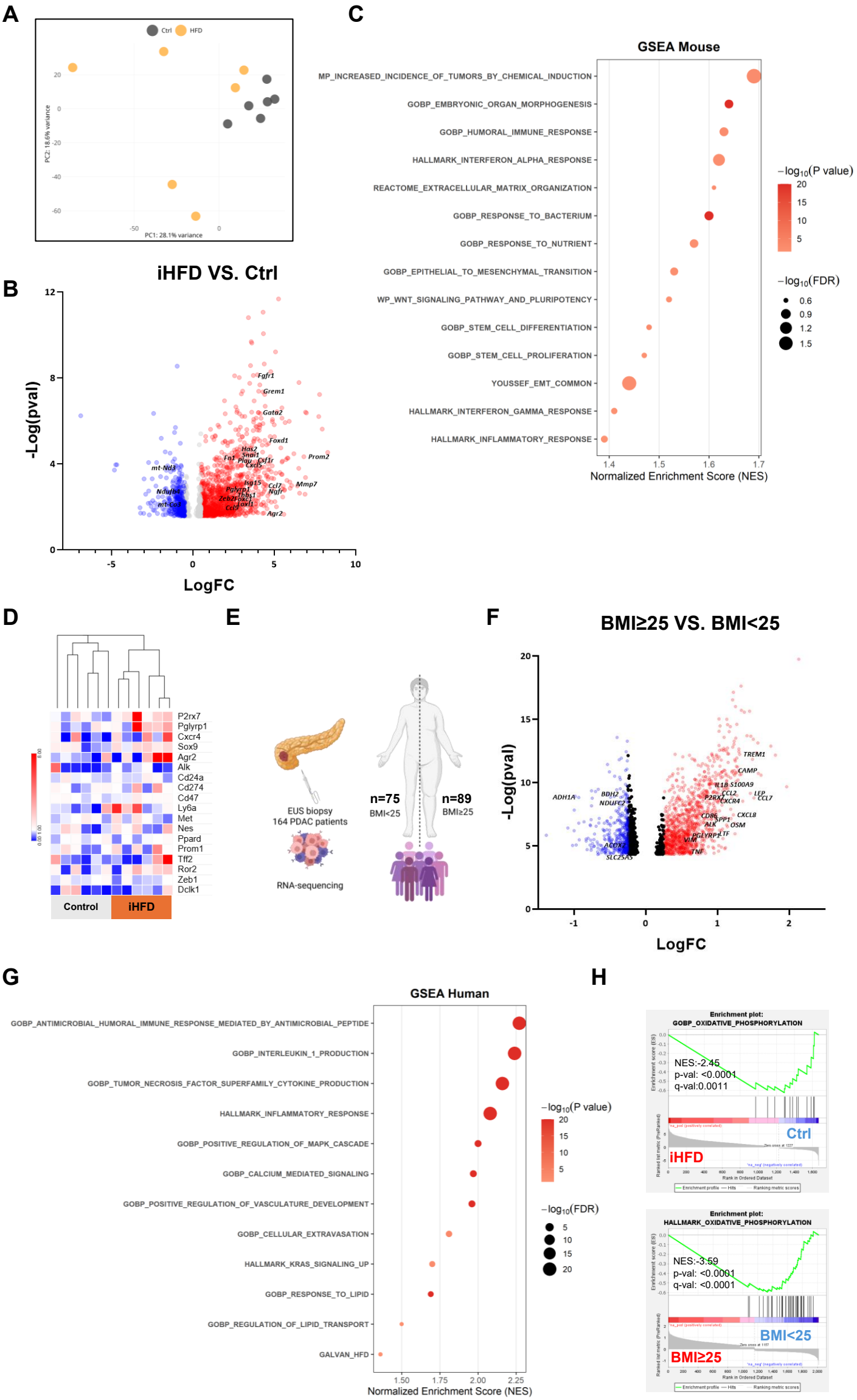
A
Ctrl
HFD
PC2: 18.6% variance
PC1: 28.1% variance
B
iHFD VS. Ctrl
-Log(pval)
LogFC
Fgfr1
Grem1
Gata2
Foxd1
Has2
Snai1
Fn1
Plau
Csf1r
Cxcl5
Prom2
mt-Nd3
Isg15
Ccl7
Mmp7
Ndufb4
Pglyrp1
Ngfr
Thbs1
Zeb2
Foxc1
mt-Co3
Ccl9
Loxl1
Agr2
C
GSEA Mouse
MP_INCREASED_INCIDENCE_OF_TUMORS_BY_CHEMICAL_INDUCTION
GOBP_EMBRYONIC_ORGAN_MORPHOGENESIS
GOBP_HUMORAL_IMMUNE_RESPONSE
HALLMARK_INTERFERON_ALPHA_RESPONSE
REACTOME_EXTRACELLULAR_MATRIX_ORGANIZATION
GOBP_RESPONSE_TO_BACTERIUM
GOBP_RESPONSE_TO_NUTRIENT
GOBP_EPITHELIAL_TO_MESENCHYMAL_TRANSITION
WP_WNT_SIGNALING_PATHWAY_AND_PLURIPOTENCY
GOBP_STEM_CELL_DIFFERENTIATION
GOBP_STEM_CELL_PROLIFERATION
YOUSSEF_EMT_COMMON
HALLMARK_INTERFERON_GAMMA_RESPONSE
HALLMARK_INFLAMMATORY_RESPONSE
Normalized Enrichment Score (NES)
−log10(P value)
−log10(FDR)
D
P2rx7
Pglyrp1
Cxcr4
Sox9
Agr2
Alk
Cd24a
Cd274
Cd47
Ly6a
Met
Nes
Ppard
Prom1
Tff2
Ror2
Zeb1
Dclk1
Control
iHFD
E
EUS biopsy
164 PDAC patients
RNA-sequencing
n=75
BMI<25
n=89
BMI≥25
F
BMI≥25 VS. BMI<25
-Log(pval)
LogFC
ADH1A
BDH2
NDUFC2
ACOX2
SLC25A5
TREM1
CAMP
IL1B
S100A9
CCL2
LEP
CCL7
P2RX7
CXCR4
CD86
CXCL8
SPP1
ALK
OSM
PGLYRP1
TF
VIM
TNF
G
GSEA Human
GOBP_ANTIMICROBIAL_HUMORAL_IMMUNE_RESPONSE_MEDIATED_BY_ANTIMICROBIAL_PEPTIDE
GOBP_INTERLEUKIN_1_PRODUCTION
GOBP_TUMOR_NECROSIS_FACTOR_SUPERFAMILY_CYTOKINE_PRODUCTION
HALLMARK_INFLAMMATORY_RESPONSE
GOBP_POSITIVE_REGULATION_OF_MAPK_CASCADE
GOBP_CALCIUM_MEDIATED_SIGNALING
GOBP_POSITIVE_REGULATION_OF_VASCULATURE_DEVELOPMENT
GOBP_CELLULAR_EXTRAVASATION
HALLMARK_KRAS_SIGNALING_UP
GOBP_RESPONSE_TO_LIPID
GOBP_REGULATION_OF_LIPID_TRANSPORT
GALVAN_HFD
Normalized Enrichment Score (NES)
−log10(P value)
−log10(FDR)
H
Enrichment plot:
GOBP_OXIDATIVE_PHOSPHORYLATION
NES:-2.45
p-val: <0.0001
q-val:0.0011
Ctrl
iHFD
Enrichment plot:
HALLMARK_OXIDATIVE_PHOSPHORYLATION
NES:-3.59
p-val: <0.0001
q-val: <0.0001
BMI<25
BMI≥25

Figure 3. Transcriptomic profile of high-fat diet-induced cell lines and PDAC patients with high body mass index (BMI). A) *Principal Component Analysis (PCA) for P21 control (Ctrl) and high-fat diet-induced (iHFD) primary tumor cell lines analyzed by RNA-seq.* ***B)*** *Volcano plot illustrating genes significantly up- (red) and downregulated (blue) in iHFD cell lines.* ***C)*** *Gene Set Enrichment Analysis (GSEA) plot showing the enrichment in the indicated pathways.* ***D)*** *Heat map showing the levels of expression as fold change of normalized counts for the indicated genes in Ctrl and HFD cell lines included in the RNA-seq analyses. The indicated genes are linked to stemness, plasticity and immune evasive phenotypes.* ***E)*** *Schematic representation of a patient comparison study involving 164 endoscopy-guided ultrasound (EUS) biopsy tumor samples, correlating BMI with tumor transcriptomic profiles. BMI cutoff has been set as 25 (n for BMI<25=75, n for BMI≥25=89).* ***F)*** *Volcano plot showing the genes significantly up- (red) and downregulated (blue) in patients with a BMI higher or equal to 25.* ***G)*** *GSEA plot showing the enrichment of the indicated pathways.* ***H)*** *GSEA plots depicting the enrichment of the oxidative phosphorylation pathway in both murine (top) and human (bottom) RNA-seq datasets.*

HFD-induced tumor cell lines present enhanced plasticity and stemness characterized by P2RX7 overexpression. To test our hypothesis regarding enriched stemness, we cultured control and iHFD cell lines as CSC-enriched spheroids. Plating an equal number of cells, iHFD cell lines formed significantly more spheroids, supporting the plastic/stem-like nature of iHFD tumor cells (**Figure 4A-B**). Next, we evaluated the expression of P2RX7 in our control and iHFD cells by RNA-seq data, qPCR and flow cytometry. P2RX7 was found consistently and significantly overexpressed in iHFD cells (**Figure 4C-F**). Moreover, we found overexpression of P2RX7 in orthotopic tumors generated in HFD-fed C57Bl/6 mice (**Figure 4G**). Given that diet-induced alterations may partially recapitulate the molecular effects of obesity, we analyzed *P2rx7* expression in an RNA-seq dataset of murine orthotopic PDAC organoids grown in HFD-fed and in leptin-deficient (ob/ob) genetic obese mice (28). Interestingly, in both models there was a significant and consistent enrichment in *P2rx7* expression compared to controls (**Figure S5A-B**), suggesting that our HFD-fed model could mimic what occurs in patients with obesity. Thus, aiming to translate these results to patients, we evaluated the expression of *P2RX7* in our cohort at the time of PDAC diagnosis, comparing patients with high and low BMI one year prior to diagnosis and at the time of diagnosis (**Figure S6A**). We found that patients with high BMI one year before PDAC diagnosis exhibited a significant enrichment of *P2RX7* expression (**Figure 4H**), but this difference disappeared at the time of the diagnosis (**Figure 4I**). This effect could be likely due to the cachexia developed during the course of the disease. Therefore, we evaluated those patients that at the time of the diagnosis were obese but lost weight, versus those that were always lean. Interestingly, those patients with high BMI one year before diagnosis retained elevated levels of *P2RX7* expression at the time of diagnosis (**Figure 4J**), even though they were

292 “lean” at that point. This finding suggests that P2RX7 may serve as a risk factor marker linking high
293 BMI to PDAC.

294 As P2RX7 is considered a CSC-associated marker, we evaluated the presence of other stem-related
295 surface markers in these cell lines. Specifically, we assessed the expression of the “highly metastatic
296 CSC population” marker CXCR4 (29) in iHFD cells and found it to be upregulated at the transcriptomic
297 and protein levels, supporting the link between HFD-induced tumors with a more invasive phenotype
298 (**Figure 4K-L**). Notably, most P2RX7-positive cells in our cultures also co-expressed CXCR4 (**Figure**
299 **4M**). We also found an increase abundance of the triple-positive (i.e., EpCAM^{+}, SCA1^{+}, CD133^{+})
300 stem-like cell population (8) in our iHFD cultures (**Figure 4N-O**). Altogether, these results position
301 HFD as an activator of plasticity and stemness in mouse PDAC. Stem-related markers such as
302 *EPCAM*, *PROM1* or *ISG15* were not differentially expressed between patients with high versus low
303 BMI one year before diagnosis (**Figure S6B-D**). However, *CXCR4* mirrored the expression pattern of
304 *P2RX7* (**Figure S6E-G**), strongly suggesting that HFD may also induce cellular plasticity and a
305 potentially metastatic phenotype in PDAC tumors.

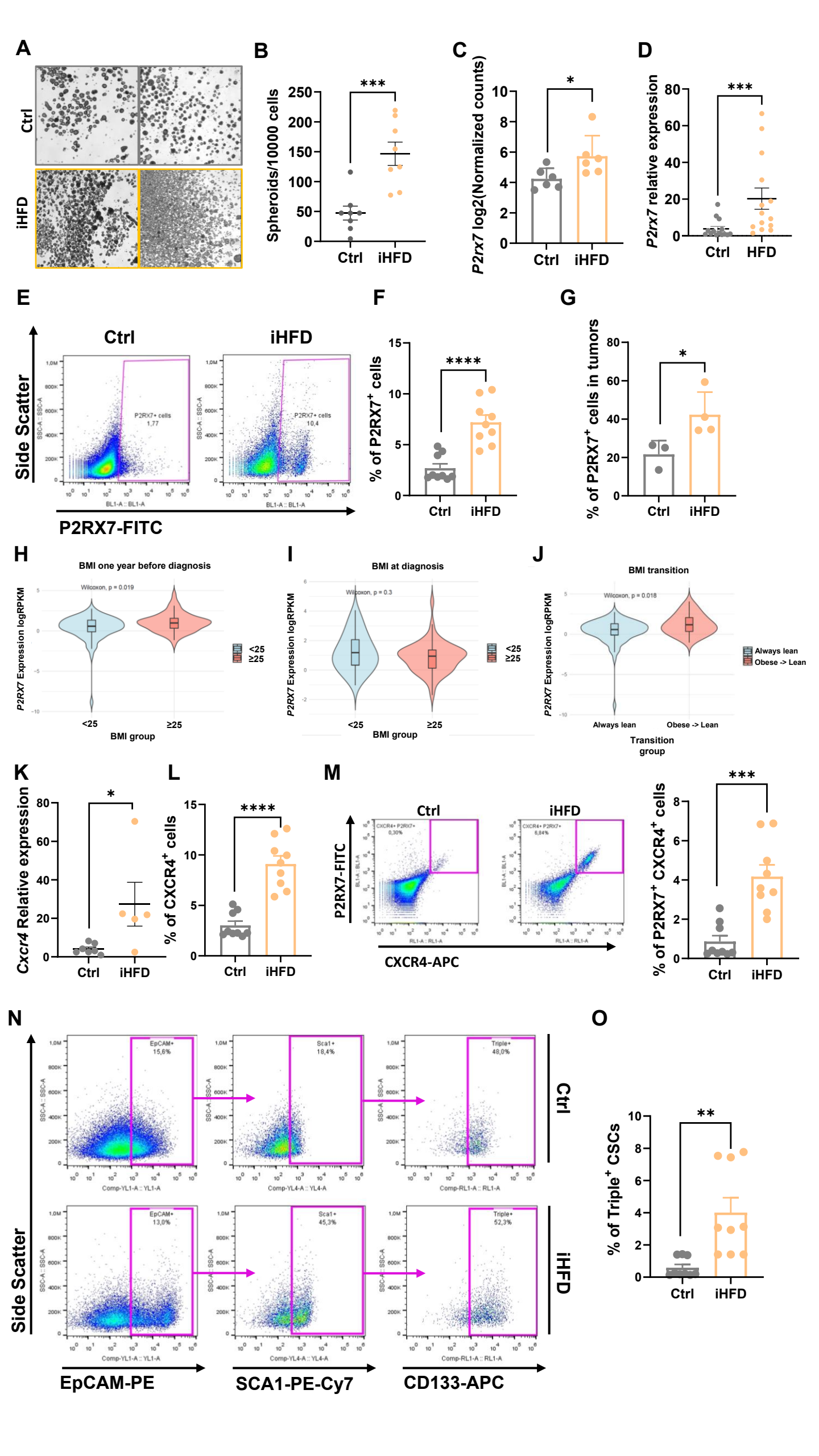
A
Ctrl
iHFD
B
Spheroids/10000 cells
***
Ctrl
iHFD
C
P2rx7 log2(Normalized counts)
*
Ctrl
iHFD
D
P2rx7 relative expression
***
Ctrl
HFD
E
Ctrl
iHFD
Side Scatter
P2RX7+ cells 1,77
P2RX7+ cells 10,4
P2RX7-FITC
F
% of P2RX7+ cells
****
Ctrl
iHFD
G
% of P2RX7+ cells in tumors
*
Ctrl
iHFD
H
BMI one year before diagnosis
Wilcoxon, p = 0.019
P2RX7 Expression logRPKM
<25
≥25
BMI group
I
BMI at diagnosis
Wilcoxon, p = 0.3
P2RX7 Expression logRPKM
<25
≥25
BMI group
J
BMI transition
Wilcoxon, p = 0.018
P2RX7 Expression logRPKM
Always lean
Obese -> Lean
Transition group
K
Cxcr4 Relative expression
*
Ctrl
iHFD
L
% of CXCR4+ cells
****
Ctrl
iHFD
M
Ctrl
iHFD
P2RX7-FITC
CXCR4-APC
% of P2RX7+ CXCR4+ cells
***
Ctrl
iHFD
N
Ctrl
iHFD
Side Scatter
EpCAM+ 15,6%
Sca1+ 18,4%
Triple+ 48,0%
EpCAM+ 13,0%
Sca1+ 45,3%
Triple+ 52,3%
EpCAM-PE
SCA1-PE-Cy7
CD133-APC
O
% of Triple+ CSCs
**
Ctrl
iHFD

307 ***Figure 4. HFD-induced cells present an enrichment in CSC markers and enhanced plasticity. A)***
308 *Representative brightfield microscopy images of spheroids generated from control (Ctrl) and high-fat diet-*
309 *induced (iHFD) primary tumor cell lines after 5 days in culture.* ***B)*** *Quantification of the number of spheroids*
310 *generated from 10000 cells. Shown is the mean ± SEM (n=8, P values as determined by unpaired T-test).* ***C)***
311 *Quantification of P2rx7 expression in Ctrl and iHFD primary cell lines from the RNA-seq analyses. Shown is the*
312 *mean ± SEM of log2(normalized counts) (n=6, P values as determined by unpaired T-test).* ***D)*** *Relative*
313 *expression of P2rx7 mRNA levels measured by RT-qPCR in Ctrl and iHFD primary tumor cell lines. Shown is*
314 *the mean ± SEM (n=14, P values as determined by unpaired T-test).* ***E-F)*** *Representative flow cytometry plots*
315 *showing the levels of P2RX7 surface expression in Ctrl and iHFD cell lines (**E**) and quantification of the*
316 *expression (**F**), shown as the mean ± SEM (n=3, P values as determined by unpaired T-test).* ***G)*** *Quantification*
317 *of the percentage of P2RX7 positive cells in tumors grown in Ctrl or iHFD-fed mice. Shown is the mean ± STDEV*
318 *(n=3, P values as determined by unpaired T-test).* ***H)*** *Violin plot showing the quantification of P2RX7 expression*
319 *in PDAC patients based on their BMI 1 year before diagnosis (n for <25=75, n for ≥25=89). P value as*
320 *determined by Wilcoxon test.* ***I)*** *Violin plot showing the quantification of P2RX7 expression in PDAC patients*
321 *based on their BMI at time of diagnosis (n for <25=35, n for ≥25=54). P value as determined by Wilcoxon test.*
322 ***J)*** *Violin plot showing the quantification of P2RX7 expression in PDAC patients based on their BMI transition*
323 *(patients previously obese that lost their weight versus those that always present a BMI<25) (n for always*
324 *<25=75, n for obese → lean =35). P value as determined by Wilcoxon test.* ***K)*** *Relative expression of Cxcr4*
325 *mRNA levels measured by RT-qPCR in Ctrl and iHFD primary tumor cell lines. Shown is the mean ± SEM (n=5,*
326 *P values as determined by unpaired T-test).* ***L)*** *Quantification of CXCR4 expression by flow cytometry in Ctrl*
327 *and iHFD primary tumor cell lines. Shown is the mean ± SEM (n=3 in triplicates, P values as determined by*
328 *unpaired T-test).* ***M)*** *Representative flow cytometry plots showing the levels of P2RX7/CXCR4 double positive*
329 *cells in Ctrl and iHFD cell lines (left panel) and quantification of the expression (right panel), shown as the mean*
330 *± SEM (n=3, P values as determined by unpaired T-test).* ***N-O)*** *Representative flow cytometry plots showing the*
331 *levels of EpCAM/SCA1/CD133 triple positive cells in Ctrl and iHFD cell lines (**N**) and quantification of the*
332 *expression (**O**), shown as the mean ± SEM (n=3, P values as determined by unpaired T-test). P values: *, <0.05;*
333 ***, <0.01; ***, <0.001; ****, <0.0001.*

334 **HFD-induced PDAC in a late adulthood model shows histological and molecular concordance**
335 **with early adulthood disease.** The HFD exposure in an early-adulthood onset revealed an important
336 role of HFD in tumor progression; however, in this model we could not address if the HFD had a role
337 in tumor induction (5, 6). As such, we next investigated whether HFD exposure could play a role in
338 tumor induction in a model resistant to tumor development. To this end, mice were kept with DOX for
339 two months, left for an additional month for DOX clearance before HFD exposure and monitored until
340 one year on a HFD diet or humane endpoint (P60 protocol). This protocol resembles adults that gain
341 mutations due to ageing or other factors and that acquire HFD-like habits later in life (**Figure 5A**).
342 Using this approach, and as expected from our previous work, control mice were resistant to tumor
343 formation (**Figure 5B-E**) (5, 6). Importantly, we found that the HFD intake led to the development of
344 lesions in 63% of the cohort, with 38% of the total mice presenting full PDAC (**Figure 5E**). Next, we
345 performed immunohistopathological analyses of these tumors and found a strong parallelism with the
346 P21 setting, including a highly mesenchymal tumor phenotype characterized by most of the cells
347 expressing vimentin and a very low proportion of cells expressing cytokeratin 19 (**Figure 5F**). iHFD
348 primary tumor-derived cell lines from the P60 protocol shared common features with iHFD P21 cell

349 lines, including a mesenchymal morphology (**Figure 5G**) and a similar expression profile, both at the
350 mRNA and protein levels for P2RX7 and CXCR4 upregulation, as well as a reduction in *Krt19* and
351 *Cdh1* expression (**Figure 5H-I**). Therefore, we found shared common features in the induction and
352 progression of a molecular mechanism in both HFD-exposed P21 and P60 protocols. Furthermore,
353 these results strongly support a critical role for HFD in two important steps of PDAC development,
354 tumor initiation and in tumor progression.

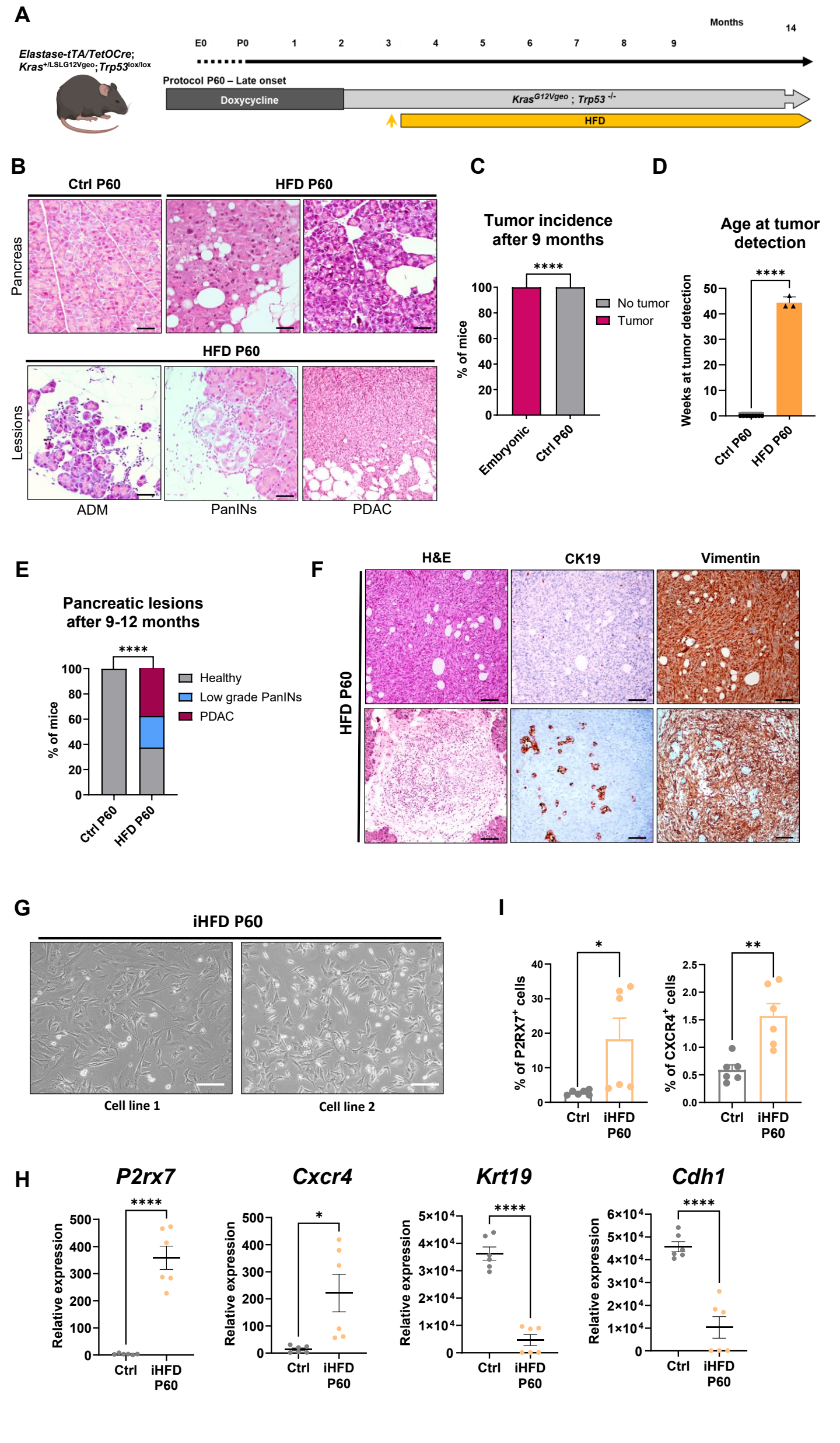
A
Elastase-tTA/TetOCre; Kras+/LSLG12Vgeo; Trp53lox/lox
Months
E0 P0 1 2 3 4 5 6 7 8 9 14
Protocol P60 – Late onset
Doxycycline
KrasG12Vgeo ; Trp53 -/-
HFD
B
Ctrl P60
HFD P60
Pancreas
HFD P60
Lesions
ADM
PanINs
PDAC
C
Tumor incidence after 9 months
****
% of mice
No tumor
Tumor
Embryonic
Ctrl P60
D
Age at tumor detection
****
Weeks at tumor detection
Ctrl P60
HFD P60
E
Pancreatic lesions after 9-12 months
****
% of mice
Healthy
Low grade PanINs
PDAC
Ctrl P60
HFD P60
F
H&E
CK19
Vimentin
HFD P60
G
iHFD P60
Cell line 1
Cell line 2
I
*
% of P2RX7+ cells
Ctrl
iHFD P60
**
% of CXCR4+ cells
Ctrl
iHFD P60
H
P2rx7
****
Relative expression
Ctrl
iHFD P60
Cxcr4
*
Relative expression
Ctrl
iHFD P60
Krt19
****
Relative expression
Ctrl
iHFD P60
Cdh1
****
Relative expression
Ctrl
iHFD P60

356 ***Figure 5. High-fat diet induces tumorigenesis in a late-onset adult PDAC mouse model and presents***
357 ***similar characteristics to the early-onset model. A)*** *Representative scheme of the protocol employed to*
358 *study the effect of high-fat diet (HFD) in late onset pancreatic cancer.* ***B)*** *Representative brightfield microscopy*
359 *images of H&E staining from pancreata at different stages of tumor development in the P60 protocol (top panel),*
360 *as well as the identified pancreatic lesions in the P60 protocol mice fed with HFD. Scale bar= 50 µm.* ***C)***
361 *Percentage of mice from embryonic (n=19) and P60 controls (Ctrl) (n=8) in which tumors were detected. P*
362 *values as determined by Chi-square test and Fisher´s exact test.* ***D)*** *Histogram showing the weeks at tumor*
363 *detection for the Ctrl (n=8) and HFD-fed (n=3) mice from the P60 protocol. Shown is the mean ± SEM (n=8*
364 *mice, P values as determined by One-way ANOVA, Tukey test).* ***E)*** *Percentage of control and HFD P60 mice*
365 *presenting healthy tissue, low grade PanINs or PDAC (n=8). P values as determined by Chi-square test and*
366 *Fisher's exact test.* ***F)*** *Representative brightfield microscopy images of hematoxylin and eosin (H&E) staining,*
367 *along with cytokeratin 19 (CK19) and vimentin IHC from two tumors generated in P60 HFD mice. Scale bar=*
368 *50 µm.* ***G)*** *Representative brightfield microscopy images of primary tumor-derived cell lines from P60 high-fat*
369 *diet-induced (iHFD) mice. Scale=300µm.* ***H)*** *Relative expression of mRNA levels measured by RT-qPCR of the*
370 *indicated genes in P21 Ctrl and P60 iHFD primary tumor cell lines. Shown is the mean ± SEM (n=2 in triplicates,*
371 *P values as determined by unpaired T-test).* ***I)*** *Quantification of P2RX7 (left panel) and CXCR4 (right panel)*
372 *expression by flow cytometry in P21 Ctrl and iHFD P60 primary tumor cell lines. Shown is the mean ± SEM*
373 *(n=2 in triplicates, P values as determined by unpaired T-test). P values: *, <0.05; **, <0.01; ***, <0.001; ****,*
374 *<0.0001.*

375

376 **HFD-derived tumor cells present enhanced metastatic capacity.** Considering the more plastic-
377 like/mesenchymal phenotype of iHFD cell lines, as well as the expression of pro-metastatic-related
378 markers (i.e., CXCR4), we evaluated the capacity of these cells to migrate and invade *in vitro* and *in*
379 *vivo.* First, we performed wound healing and transwell invasion assays comparing the migratory
380 capacity and invasiveness of control and iHFD cells. In both cases, iHFD cell lines presented an
381 enhanced ability to close wounds and to migrate through Matrigel™ (**Figure 6A-D**). We next
382 evaluated the presence of spontaneous metastases in our GEMMs. As P60 control mice did not form
383 primary tumors or lesions, we focused on the embryonic and P21 protocols. We found that in the P21
384 protocol, 22.22% of control mice presented liver metastases, while 71.43% of the HFD mice presented
385 both liver and/or lung metastases, showing a pro-metastatic impact of the HFD (**Figure 6E, G**). Due
386 to the aggressive nature and rapid development of primary PDAC tumors in the embryonic model,
387 none of the control mice presented metastases, but in the HFD-exposed embryonic model, we found
388 that 54.54% of mice presented metastases in the liver and lung at humane end point (**Figure 6F-G**).
389 Thus, in general, for both protocols, we found that HFD induced more metastatic burden and primed
390 cells to both the lung and liver (**Figure 6H**).

391 To further validate that the pro-metastatic effect of HFD is imprinted in tumor cells, we performed an
392 intrasplenic experimental metastasis assay in C57Bl/6 mice with control and iHFD cell lines to
393 evaluate their capacity to generate liver metastasis (**Figure 6I**). After three weeks, we sacrificed the

394 mice and found that all iHFD cell lines colonized the liver and produced metastasis, while the controls
395 cell lines did not (**Figure 6J**). Considering that HFD-induced fatty liver could be a better soil for
396 metastatic seeding (30), we evaluated the capacity of control cell lines to metastasize in mice fed with
397 normal diet or HFD (**Figure S7A-B**). Although we did not find an increased metastatic burden in HFD-
398 fed mice (**Figure S7C-D**), we observed that the EpCAM+ cells found in the liver were mainly P2RX7+,
399 suggesting the implication of this receptor in metastatic seeding (**Figure S7E**). To validate this
400 observation in a human setting, we interrogated an already annotated single cell RNA-seq dataset
401 comprising 12 matched samples from primary tumors and liver metastases (31) (**Figure 6K**). *P2RX7*
402 expression was mainly restricted to the immune compartment both in primary tumor and metastasis
403 (**Figure 6L**); however, we found a small proportion of cells in the epithelial compartment expressing
404 the gene, as expected from for CSC marker (**Figure 6M**). In line with our results in mouse models,
405 we found that metastasis presented a higher proportion of P2RX7-expressing tumor cells compared
406 to primary tumors (**Figure 6N**). Altogether, these results support that HFD induces a metastatic
407 phenotype in tumor cells characterized by P2RX7-expression during tumor evolution.

408
409
410
411
412
413

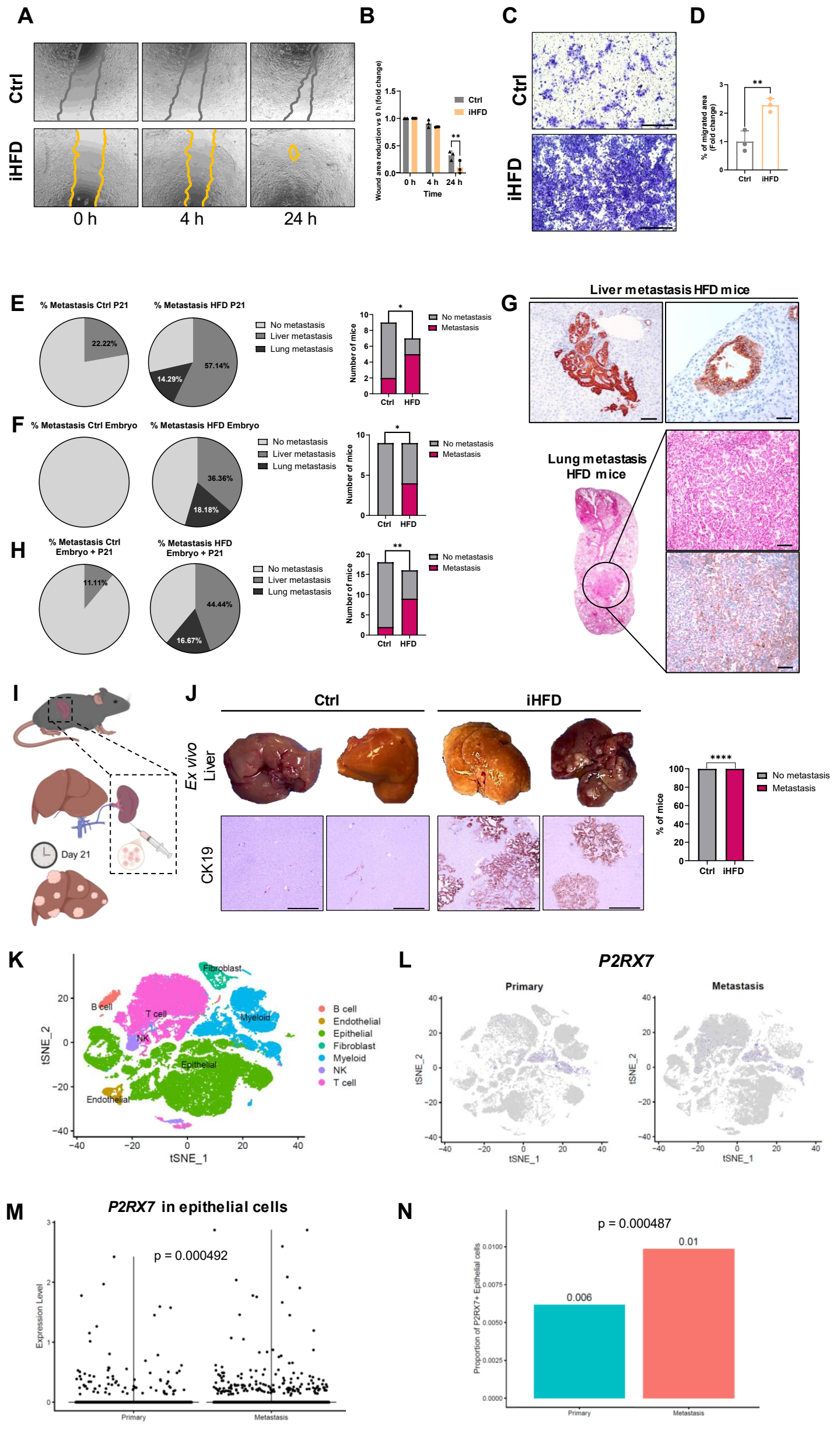
A
Ctrl
iHFD
0 h
4 h
24 h
B
Wound area reduction vs 0 h (fold change)
Ctrl
iHFD
0 h
4 h
24 h
Time
C
Ctrl
iHFD
D
% of migrated area (Fold change)
Ctrl
iHFD
E
% Metastasis Ctrl P21
% Metastasis HFD P21
22.22%
57.14%
14.29%
No metastasis
Liver metastasis
Lung metastasis
Number of mice
Ctrl
HFD
Metastasis
F
% Metastasis Ctrl Embryo
% Metastasis HFD Embryo
36.36%
18.18%
G
Liver metastasis HFD mice
Lung metastasis HFD mice
H
% Metastasis Ctrl Embryo + P21
% Metastasis HFD Embryo + P21
11.11%
44.44%
16.67%
I
Day 21
J
Ctrl
iHFD
Ex vivo
Liver
CK19
% of mice
K
Fibroblast
B cell
T cell
Myeloid
NK
Epithelial
Endothelial
tSNE_1
tSNE_2
L
P2RX7
Primary
Metastasis
M
P2RX7 in epithelial cells
p = 0.000492
Expression Level
Primary
Metastasis
N
p = 0.000487
0.006
0.01
Proportion of P2RX7+ Epithelial cells

415 ***Figure 6. High-fat diet induces a pro-metastatic phenotype. A)*** *Representative brightfield microscopy*
416 *images of wound healing assays at 0-, 4- and 24-hours post-scratch in both control (Ctrl) and high-fat diet-*
417 *induced (iHFD) cell lines.* ***B)*** *Quantification of wound area reduction shown in A represented as the mean fold*
418 *change ± STDEV with time 0h set as 1.0 (n=3, P values as determined by unpaired T-test).* ***C)*** *Representative*
419 *brightfield microscopy images of crystal violet-stained transwell migration assays at 24 hours post-seeding in*
420 *both Ctrl and iHFD cell lines.* ***D)*** *Quantification of migration area shown as the mean fold change ± STDEV with*
421 *Ctrl cell lines set as 1.0 (n=3, P values as determined by unpaired T-test).* ***E)*** *Left panel: Proportion plots showing*
422 *the percentage of Ctrl and iHFD mice with metastasis from the P21 protocol. Right panel: Quantification of the*
423 *number of mice with metastasis in both conditions (n=9 in Ctrl and 7 in HFD, P values as determined by Chi-*
424 *square test).* ***F)*** *Left panel: Proportion plots showing the percentage of Ctrl and HFD mice with metastasis from*
425 *the embryonic (Embryo) model. Right panel: Quantification of the number of mice presenting metastasis in both*
426 *conditions (n=9 in Ctrl and 9 in HFD, P values as determined by Chi-square test).* ***G)*** *Representative brightfield*
427 *microscopy images from cytokeratin 19 immunohistochemistry-stained and H&E-stained samples from*
428 *metastatic disease in HFD mice from the P21 protocol in liver (top panel) and lung (bottom panel). Scale bar=*
429 *500 µm.* ***H)*** *Left panel: Proportion plots showing the percentage of Ctrl and HFD mice from both models*
430 *(embryonic and adult P21), which present metastasis. Right panel: Quantification of the number of mice*
431 *presenting metastasis in both conditions (n=18 in Ctrl and 16 in HFD, P values as determined by Chi-square*
432 *and Fisher´s exact test).* ***I)*** *Graphical scheme showing the basis of the intrasplenic assay to evaluate the liver*
433 *metastatic capacity of a cell line.* ***J)*** *Left panel: Representative pictures of livers from the intrasplenic assay*
434 *injected with Ctrl and iHFD cell lines (top) and representative brightfield microscopy images from cytokeratin 19*
435 *(CK19) immunohistochemistry of Ctrl and HFD livers (bottom). Right panel: Quantification of the percentage of*
436 *mice that showed macroscopic metastasis in the intrasplenic assay (n=3 cell lines per condition, P values as*
437 *determined by Chi-square and Fisher´s exact test).* ***K)*** *tSNE plot showing the different annotated cell types from*
438 *the Liu et al. (31) single cell RNA-seq dataset of human primary tumors and metastasis.* ***L)*** *tSNE plots showing*
439 *the P2RX7-expressing (blue) cells in the Liu et al. dataset separated by condition (primary for primary tumor*
440 *and metastasis for liver metastasis).* ***M)*** *Quantification of P2RX7 expression in the epithelial compartment in*
441 *both primary tumor and metastasis. P value indicated and determined by Wilcoxon test.* ***N)*** *Bar plot of P2RX7-*
442 *expressing cells in primary tumors and metastasis. P value indicated and determined by Fisher test. P values:*
443 **, <0.05; **, <0.01; ***, <0.001; ****, <0.0001.*

444

445 **Lipid-conditioned macrophages drive plasticity in tumor cells through a CAMP-P2RX7 axis.**

446 We next studied the mechanisms by which HFD induces the mesenchymal/plastic phenotype of tumor
447 cells. Since fatty acids (FAs) have been reported to induce a pro-CSC phenotype in human tumor
448 cells (32), we asked whether increase exposure to FAs could cause the observed phenotype.
449 Regarding P2RX7 expression, none of the FAs we tested (oleic acid, monounsaturated; linoleic acid,
450 polyunsaturated; palmitic acid, saturated) could increase P2RX7 levels in mouse control cell lines
451 (**Figure 7A**) or in PDX-derived human primary cell lines (**Figure 7B**). Thus, we hypothesized that the
452 increase in P2RX7 and the phenotype induction could be driven by components of the tumor
453 microenvironment such as adipose tissue or neutrophils (9). To test this hypothesis, we cultured
454 adipose tissue from regular diet and HFD-fed C57Bl/6 mice and obtained adipose tissue conditioned
455 medium (ACM). Exposure of control cell lines to ACM did not result in an increase in P2RX7 (**Figure**
456 **7C**). Also, we found that neutrophils were poorly infiltrated or almost absent in HFD tumors (**Figure**
457 **S8A-B**). Next, we assessed highly tumor infiltrating macrophages, although they were not significantly

458 different in both settings (**Figure S8A, C**). Importantly, since the human RNA-seq data revealed an
459 enrichment in gene signatures for lipid-conditioned macrophages and antimicrobial response, we
460 theorized that macrophages might influence *P2RX7* expression in tumor cells and activate it via its
461 ligand, CAMP. Indeed, *P2RX7* and *CAMP* positively correlated in human PDAC (**Figure 7D**) and
462 CAMP expression has been linked to metabolic diseases related to obesity such as atherosclerosis
463 or diabetes (33, 34). To address this, we cultured immortalized primary bone marrow-derived
464 macrophages (IBMDMs) with FAs, and measured *Camp* expression at the transcriptomic level. We
465 found that naive IBMDMs did not express *Camp*, whereas FAs stimulation robustly induced its
466 expression (**Figure 7E**). Importantly, mice fed with HFD presented increase CAMP-expressing
467 macrophages in the bone marrow (BM) and intratumorally compared to control mice (**Figure 7F-G**).
468 As it was described that macrophage-derived hCAP-18/LL-37 can induce P2RX7 expression in
469 human cell lines (19), we next cultured control cells with naive macrophages conditioned medium
470 (MCM) or FAs-treated macrophage conditioned medium (F-MCM). Interestingly, F-MCM induced
471 more the expression levels of *P2rx7* compared to control cell lines treated with MCM (**Figure 7H**).
472 Furthermore, F-MCM decreased *Epcam* expression levels (**Figure 7I**) and induced a more
473 mesenchymal phenotype (**Figure 7J**), supporting that FAs derived from the diet conditioned
474 macrophages to produce molecules, such as CAMP, that induce P2RX7 expression and changes in
475 the cellular phenotype. Notably, stimulation of control cell lines with recombinant CAMP (rCAMP)
476 increased the levels of P2RX7 and CXCR4 (**Figure 7K-L**). In addition, we evaluated whether rCAMP
477 could also account for the elevated expression of PGLYRP1 observed in iHFD cells (**Figure S9A**).
478 We found that rCAMP significantly increased PGLYRP1 expression levels in control cell lines (**Figure**
479 **S9B**). Due to the protective role of PGLYRP1 blocking macrophage phagocytosis in PDAC cells (8),
480 we next performed a phagocytosis assay to determine whether iHFD cells exhibit enhanced protection
481 and immune evasive features. Consistent with the overexpression of PGLYRP1, iHFD cell lines were
482 phagocytosed less efficiently by primary macrophages than control cell lines (**Figure S9C-D**).

483 After finding an increase in CAMP expression in murine BM macrophages, we evaluated its
484 expression in patients' PBMCs as a possible proxy marker for HFD-induced PDAC. Although

485 macrophages are not present in circulation, we detected *CAMP* expression in PBMCs from both
486 patients and non PDAC controls (**Figure S10A-B**). As this circulating CAMP is unlikely to be
487 macrophage derived, no significant differences were observed between groups stratified by BMI.
488 However, in both groups (BMI<25 and BMI>25), PDAC patients exhibited higher *CAMP* expression
489 in PBMCs compared with non-PDAC controls (**Figure S10C-D**). As a complementary approach, we
490 assessed the serum levels of the hCAP-18-derived peptide LL-37 in a cohort of healthy donors and
491 PDAC patients. We found that PDAC patients with locally advanced and metastatic disease presented
492 increased levels of sera LL-37, compared with healthy donors (**Figure 7M**). When we divided PDAC
493 patients according to their BMI and compared the highest and lowest quartiles of the cohort, we found
494 higher levels in those with high BMI (**Figure 7N**). These distinctions became more evident upon
495 assessing *CAMP* expression at the transcriptomic level in patients, where we observed a parallel
496 trend with *P2RX7* and *CXCR4* expression; specifically, increased levels among individuals with high
497 BMI one year prior to diagnosis (**Figure 7O-Q**). Finally, we also evaluated EpCAM and hCAP-18/LL-
498 37 levels by immunohistochemistry in a small patient cohort divided by BMI. In line with our results,
499 patients with BMI>25 displayed lower EpCAM expression in tumor cells and higher levels of LL-37
500 within the immune compartment compared to patients with BMI<25 (**Figure S11A-C**). Altogether,
501 these results support that HFD-induced obesity induces the systemic expression of CAMP by
502 macrophages, which may contribute to the induction of an immune evasive and more mesenchymal
503 plastic tumor cell state within the tumor.

504

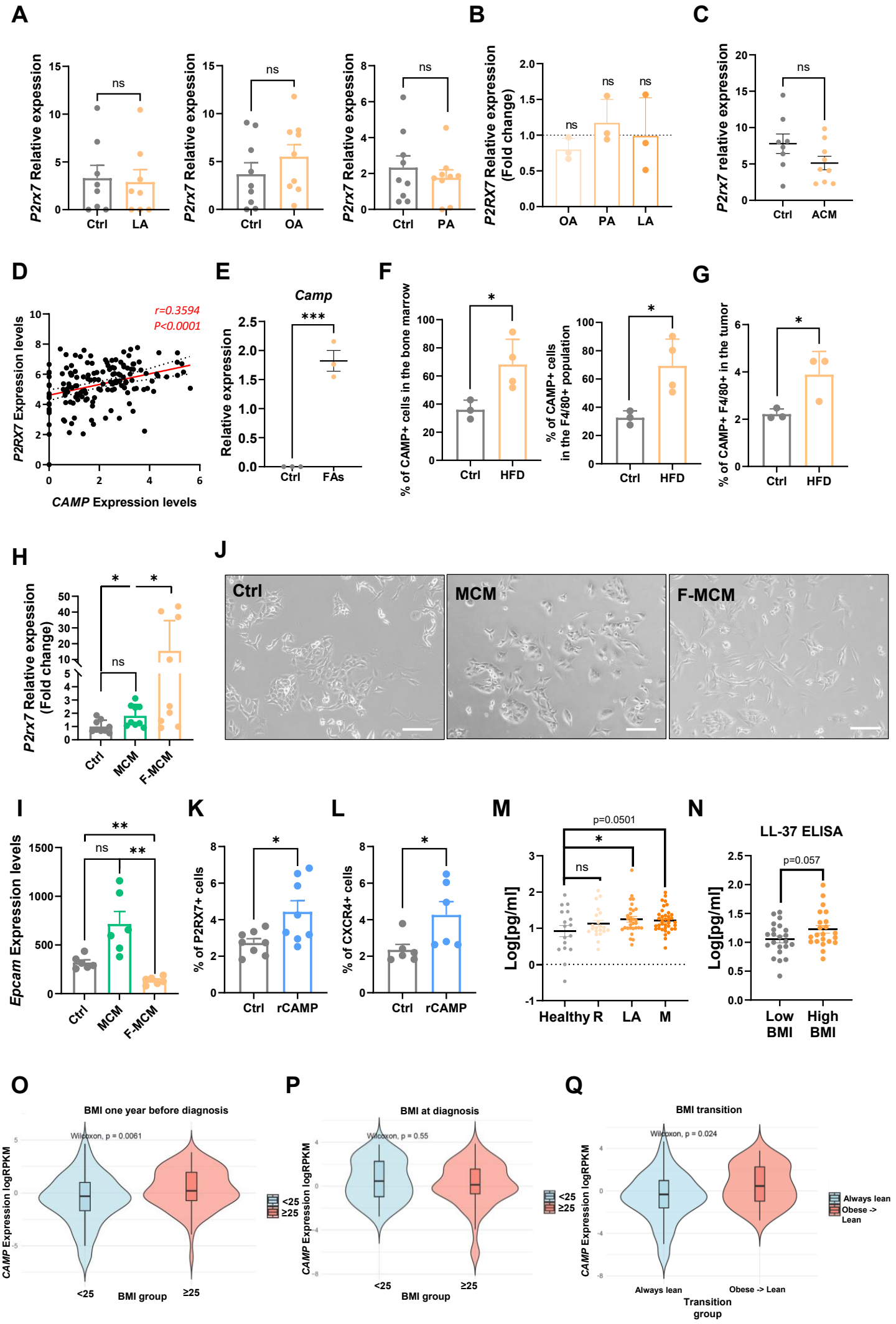
A
P2rx7 Relative expression
ns
Ctrl
LA
OA
PA
B
P2RX7 Relative expression (Fold change)
OA
PA
LA
C
P2rx7 relative expression
Ctrl
ACM
D
P2RX7 Expression levels
CAMP Expression levels
r=0.3594
P<0.0001
E
Camp
Relative expression
***
Ctrl
FAs
F
% of CAMP+ cells in the bone marrow
% of CAMP+ cells in the F4/80+ population
*
Ctrl
HFD
G
% of CAMP+ F4/80+ in the tumor
H
P2rx7 Relative expression (Fold change)
Ctrl
MCM
F-MCM
J
Ctrl
MCM
F-MCM
I
Epcam Expression levels
**
K
% of P2RX7+ cells
rCAMP
L
% of CXCR4+ cells
M
p=0.0501
Log[pg/ml]
Healthy R
LA
M
N
LL-37 ELISA
p=0.057
Low BMI
High BMI
O
BMI one year before diagnosis
Wilcoxon, p = 0.0061
CAMP Expression logRPKM
<25
≥25
BMI group
P
BMI at diagnosis
Wilcoxon, p = 0.55
Q
BMI transition
Wilcoxon, p = 0.024
Always lean
Obese -> Lean
Transition group

506 ***Figure 7. P2RX7-CAMP axis is induced by macrophages. A)*** *Quantification of P2rx7 expression by RT-qPCR*
507 *in control (Ctrl) murine cell lines treated with fatty acids (FAs) (linolenic acid, LA [200μM]; oleic acid, OA [50μM];*
508 *palmitic acid, PA [50μM sodium palmitate]). Shown is the mean ± SEM (n=4 cell lines in duplicates for LA, and*
509 *3 cell lines in triplicate for OA and PA, P values as determined by unpaired T-test).* ***B)*** *Quantification of P2RX7*
510 *expression by RT-qPCR in PDX-derived primary human cell lines treated with FAs. Shown is the mean fold*
511 *change ± SEM with controls set as 1.0 (n=3 cell lines, P values as determined by unpaired T-test).* ***C)***
512 *Quantification of P2rx7 expression by RT-qPCR in Ctrl murine cell lines treated with adipose tissue conditioned*
513 *medium (ACM) for 48 hours. Shown is the mean ± SEM (n=4 cell lines in duplicates, P values as determined*
514 *by unpaired T-test).* ***D)*** *Dot plot showing the correlation between P2RX7 and CAMP expression in TCGA*
515 *patients. P values and r were calculated by Pearson's correlation.* ***E)*** *Quantification of Camp expression by RT-*
516 *qPCR in immortalized bone marrow-derived macrophages treated with FAs (linolenic acid, LA; oleic acid, OA;*
517 *palmitic acid, PA). Shown is the mean ± STDEV (n=3, P values as determined by unpaired T-test).* ***F)***
518 *Quantification of CAMP positive total cells (left panel) and CAMP positive cells in macrophages (F4/80) (right*
519 *panel) from the bone marrow determined by flow cytometry in mice fed with Ctrl diet and HFD. Shown is the*
520 *mean ± STDEV (n=3 mice for control group, 4 for HFD group, P values as determined by unpaired T-test).* ***G)***
521 *Quantification of CAMP positive tumor-associated macrophages determined by flow cytometry in mice fed with*
522 *Ctrl diet and HFD. Shown is the mean ± STDEV (n=3 mice, P values as determined by unpaired T-test).* ***H)***
523 *Quantification of P2rx7 expression by RT-qPCR in Ctrl murine cell lines treated with macrophage conditioned*
524 *medium (MCM) or fatty acid-trained macrophage conditioned medium (F-MCM) for 48 hours. Shown is the*
525 *mean fold change ± SEM with Ctrl set as 1.0 (n=3 cell lines in triplicates, P values as determined by One Way*
526 *ANOVA).* ***I)*** *Quantification of Epcam expression by RT-qPCR in Ctrl murine cell lines treated with MCM or F-*
527 *MCM for 48 hours. Shown is the mean fold change ± SEM with Ctrl set as 1.0 (n=3 cell lines in duplicates, P*
528 *values as determined by One Way ANOVA).* ***J)*** *Representative brightfield microscopy images of Ctrl cells*
529 *treated with MCM and F-MCM. Scale bar= 50μm.* ***K)*** *Quantification of P2RX7 positive cells determined by flow*
530 *cytometry in a Ctrl cell culture treated with recombinant (r) CAMP (100 μg/mL) for 48 hours. Shown is the mean*
531 *± SEM (n=8, P values as determined by unpaired T-test).* ***L)*** *Quantification of CXCR4 positive cells determined*
532 *by flow cytometry in a Ctrl cell culture treated with rCAMP (100 μg/mL) for 48 hours. Shown is the mean ± SEM*
533 *(n=6, P values as determined by unpaired T-test).* ***M)*** *Quantification by ELISA of soluble LL-37 levels in sera*
534 *from healthy donors (Healthy) (n=17) and PDAC patients with resectable (R) (n=21), locally advanced (LA)*
535 *(n=30) or metastatic disease (M) (n=37). Shown is the mean of log normalized concentration ± SEM (P values*
536 *as determined by One-Way ANOVA, Dunnet's test).* ***N)*** *Quantification by ELISA of soluble LL-37 levels in sera*
537 *from PDAC patients from the highest and lowest quartiles of BMI (n=22 patients per condition). Shown is the*
538 *mean of log normalized concentration ± SEM (P values as determined by unpaired T-test).* ***O)*** *Violin plot showing*
539 *the quantification of CAMP expression in PDAC patients based on their BMI 1 year before diagnosis (n for*
540 *<25=75, n for ≥25=89). P value as determined by Wilcoxon test.* ***P)*** *Violin plot showing the quantification of*
541 *CAMP expression in PDAC patients based on their BMI at time of diagnosis (n for <25=35, n for ≥25=54). P*
542 *value as determined by Wilcoxon test.* ***Q)*** *Violin plot showing the quantification of CAMP expression in PDAC*
543 *patients based on their BMI transition (patients previously obese that lost their weight versus those that always*
544 *present a BMI<25) (n for always <25=75, n for obese → lean =35). P value as determined by Wilcoxon test. P*
545 *values: *, <0.05; **, <0.01; ***, <0.001; ****, <0.0001.*

546

547 **Discussion**

548 Mouse models of PDAC have been instrumental over the past decade for preclinical studies, enabling
549 the field to capture the complexity of a disease in which the tumor microenvironment plays a central
550 role. Among them, the KPC model (*Pdx1/Ptf1a*-Cre; *Kras*$^{+/G12D}$; *Trp53*$^{mut\ or\ KO}$) has been widely used
551 (35), yet, like all models, it presents inherent limitations. The acquisition of oncogenic mutations during
552 embryonic development generates tumors that mimic key features of human PDAC. However, in
553 humans, these mutations are not acquired during embryonic development and this could be the
554 reason why it has been suggested that mutations are not sufficient to drive PDAC (36-38). Indeed,

555 Carpenter *et al.* recently demonstrated that healthy individuals frequently harbor *KRAS*-mutant
556 PanINs (4), and the prevalence of these lesions far exceeds the incidence of PDAC. This strongly
557 suggests that oncogenic potential does not reside solely in mutations but requires additional events,
558 particularly chronic inflammation, to initiate tumorigenesis.

559 Multiple studies over the past two decades have linked inflammatory cues to PDAC initiation and
560 progression, whether through epigenetic priming (39, 40), microenvironmental remodeling (41, 42) or,
561 as our group previously showed, through tissue damage that propagates oncogenic signaling and
562 suppresses senescence (5, 6). To dissect these processes, we developed inducible mouse models
563 in which mutations arise specifically in the acinar compartment of adult mice using a Tet-Off system.
564 This KPeC model (*Elas-tTA/tetO-Cre*; *Kras*$^{+/LSL}$G12Vgeo; *Trp53*$^{lox/lox}$) revealed that the adult pancreas is
565 intrinsically resistant to oncogenic transformation and that chronic pancreatitis is required to overcome
566 this barrier, a concept now widely accepted in the human setting. Importantly, this model provides a
567 unique opportunity to interrogate “early-onset” and “late-onset” PDAC, which we modelled through
568 our P21 and P60 protocols.

569 The rising incidence of PDAC in individuals under 50 years of age (3) suggests that environmental
570 exposures, including diet, may play a major role. By inducing mutations at different ages, we observed
571 that younger hosts were more permissive to tumor formation than the adult pancreas, which was
572 completely resistant to transformation by the *Kras* oncogene expression and *Trp53* loss, as previously
573 reported (5). This may reflect the retention of plasticity or stem-like features within subsets of acinar
574 cells, traits that become progressively restricted with age (43-45).

575 Strikingly, we found that HFD consumption increased tumor aggressiveness, metastatic behavior, and
576 reduced survival in the P21 protocol. These findings led us to hypothesize that chronic HFD exposure,
577 particularly during childhood or early adulthood, creates a systemic inflammatory landscape that
578 facilitates oncogenic transformation once mutations arise. Supporting this idea, we observed that
579 HFD-induced systemic signaling imprints stable transcriptional changes in tumor cells that persist in
580 culture, likely through epigenetic mechanisms. The acquisition of a plastic, stem-like phenotype,
581 robustly preserved in iHFD cell lines, has important clinical implications, as such states are strongly

582 associated with therapy resistance and metastatic behavior (46-49). Notably, this phenotype has not
583 been previously described in HFD-fed PDAC models.

584 Noteworthy, in our late-onset protocol (P60) we could induce preneoplastic lesions and full tumors in
585 a model that is normally resistant to the disease. This shows for the first time a link between specific
586 dietary habits and tumor induction in a model that presents oncogenic mutations at this age stage. In
587 alignment with our results with the P21 protocol, HFD-induced tumors and tumor cell lines both
588 presented a mesenchymal histology and morphology, as well as an enrichment in plastic-like cells
589 characterized by the expression of P2RX7 and CXCR4. These results strongly support the effect of
590 diet in the molecular characteristics and dynamics of PDAC formation and evolution despite the age
591 of mutation acquisition.

592 Although other inducible KRAS models have been used to study the intersection between HFD and
593 PDAC, they often rely on protocols that do not account for age-dependent differences in acinar cell
594 susceptibility to transformation (9, 10). These studies attributed the tumor-promoting effects of HFD
595 to enhanced desmoplasia, collagen deposition, and inflammation mediated by COX2 and IL-1β,
596 implicating pancreatic stellate cells, neutrophils, and adipocytes as key drivers. In contrast, our
597 models did not support a major role for neutrophils or adipose tissue. Instead, macrophages emerged
598 as central regulators of the tumor cell state observed both *in vitro* and *in vivo*. These discrepancies
599 may reflect differences in model design or the extended tracking period in our study, which spanned
600 up to one year. Importantly, the morphological and transcriptional reprogramming toward a
601 mesenchymal/plastic-like state had not been previously reported. Moreover, our analysis of real-world
602 patient data corroborated these findings, reinforcing their clinical relevance. Collectively, these
603 observations highlight HFD-induced obesity as a critical variable that should be considered when
604 studying interpatient PDAC heterogeneity and raises the question of whether dietary interventions
605 could reverse or mitigate this acquired phenotype.

606 Mechanistically, we show that FAs systemically condition macrophages to produce CAMP. In humans,
607 macrophage-derived hCAP-18 (the human homolog of murine CAMP) and its active peptide LL-37
608 have been shown to activate the CSC compartment in PDAC and contribute to tumorigenesis (19).

609 We found that both CAMP and its receptor P2RX7 were upregulated in patients with high BMI and in
610 HFD-derived tumors. Furthermore, CAMP induced the expression of PGLYRP1, another antimicrobial
611 protein produced by neutrophils and CSCs that protects tumor cells from macrophage- and
612 T-cell-mediated elimination (8). This CAMP–P2RX7–PGLYRP1 axis not only reinforces the plastic,
613 stem-like state of HFD-induced tumor cells but also shields them from immune clearance and
614 promotes metastatic behavior.

615 Consistent with this, we found that HFD enhances metastasis in a tumor cell-intrinsic manner. In this
616 context, the "seed" acquires the capacity to colonize distinct environments (lung and liver)
617 independently of the host, as HFD-fed mice did not exhibit increased metastasis when injected with
618 control cell lines in an intrasplenic assay. Notably, metastatic EpCAM^{+} tumor cells consistently
619 expressed high levels of P2RX7, underscoring its importance for metastatic success, a role previously
620 described in melanoma and prostate cancer (50, 51). Interestingly, in colorectal cancer the P2RX7–
621 CAMP axis appears to function in the opposite direction (52), highlighting the context-specific nature
622 of this pathway.

623 Although further research is needed, our findings position P2RX7 as a central driver of HFD- and
624 obesity-related PDAC, opening the door to more personalized therapeutic strategies for this patient
625 subgroup. Circulating hCAP-18/LL-37 may be a potential biomarker for early PDAC detection and
626 identifying candidates for targeted therapy. However, our analysis showed minor differences in LL-37
627 serum levels compared to RNA-seq results. This phenomenon may be attributed to the possibility that
628 patients with elevated BMI one year prior to diagnosis are misclassified as having low BMI at the time
629 of diagnosis due to disease-related weight loss. Thus, proper clinical data management seems to be
630 crucial to properly assess these changes.

631 In conclusion, here we describe the effects of HFD in tumor development in novel early onset and late
632 onset protocols for PDAC GEMMs. Our results show that diet could influence the transcriptional state
633 of tumor cells, rendering them a more stem/plastic-like state, which favors the metastatic disease.
634 HFD induces the expression of P2RX7, which is activated via macrophage-derived CAMP and favors
635 this characteristic tumor cell state. In patients, high BMI correlates with *P2RX7* and *CAMP* expression,

636 as well as the metastatic marker *CXCR4*, and it is preserved despite weight loss during disease
637 evolution. Altogether, these findings not only reveal a diet- and obesity-driven mechanism that shapes
638 tumor cell plasticity and metastatic potential but also highlights P2RX7 and CAMP as actionable
639 biomarkers and therapeutic targets, paving the way for early detection, risk stratification, and
640 personalized interventions in PDAC patients.

641 **Materials and methods**

642 ***Mice.*** The *Kras*$^{+/LSLG12Vgeo}$;*Elas-tTA/tetO-Cre* (53) and the *Trp53*$^{lox/lox}$ (54) strains have been previously
643 described. The *Elas-tTA/tetO-Cre* transgenes drive expression of the bacterial Cre recombinase from
644 the *Elastase* promoter under the negative control of doxycycline (DOX) (Tet-off system). For the
645 postnatal adult protocols, DOX (2 mg/ml, Sigma Cat no. D3447) was provided in the drinking water
646 as a sucrose (5% w/v) solution to pregnant mothers (from the time of conception) and to their offspring
647 until the time required to allow expression of the Cre recombinase. For the early onset adulthood
648 protocol, mice were exposed to doxycycline until 3 weeks of age and then fed a HFD 60%
649 (Brogaarden, Cat no. D12492I) ad libitum or normal chow diet until 1 year or humane endpoint. For
650 the late onset adulthood protocol, mice were exposed to doxycycline until 8 weeks and at 12 weeks
651 of age were fed a HFD or normal chow diet until 1 year or humane endpoint (**Figure 1A**). Both female
652 and male mice were used for all experiments and body weight was monitored weekly. Necropsies
653 were performed in the dissection laboratory of the CNIO Animal Facility. Mice were euthanized in a
654 CO_2 chamber and tissue samples (pancreas, tumor, metastases, liver, lungs, intestine, white and
655 brown adipose tissue, spleen, kidney) were collected in 10% buffered formalin for histopathology. All
656 animal experiments were carried out in the animal facility of the CNIO and were approved by the
657 Ethical Committee of the CNIO and the Institute of Health Carlos III (PROEX 286.8/23). Mice were
658 genotyped by Transnetyx (Tennessee, USA).

659 ***Intrasplenic metastasis assay.*** For intrasplenic implantation, a total of 250,000 cells were
660 resuspended in 50 µL of phosphate-buffered saline (PBS; Gibco, USA). Mice were anesthetized with
661 4% isoflurane (Braun Vetcare, Germany) in 100% oxygen at a flow rate of 1.5 L/min and received
662 preoperative analgesia with buprenorphine as well as ophthalmic protection with Lacryvisc gel (Alcon,

663 Switzerland). Body temperature was maintained using heated beds throughout the procedure.
664 Following removal of abdominal hair, a small incision was made on the left flank to expose the spleen.
665 The cell suspension was injected directly into the splenic parenchyma using 30-gauge insulin
666 syringes. The peritoneal wall was closed with absorbable Vicryl sutures (Ethicon Inc., USA), and the
667 skin was sealed with wound clips (CellPoint Scientific Inc., USA). Tumor progression was monitored
668 weekly by abdominal ultrasound. After 21 days, mice were euthanized and tissue samples collected
669 for the analysis of liver metastases.

670 ***Tumor monitorization.*** Tumor development was assessed by weekly palpation and by ultrasound
671 imaging performed once per month. After tumor detection, ultrasound monitoring was conducted
672 weekly at the Molecular Imaging Core Unit of CNIO. For imaging, mice were anesthetized with 3%
673 isoflurane (Braun Vetcare, Germany) delivered in 100% oxygen at a flow rate of 0.5 L/min. Bed
674 heaters were used to avoid hypothermia due to the anesthesia and abdominal hair was locally
675 removed. Tumor measurements were obtained using a high-resolution Vevo 770 ultrasound system
676 (VisualSonics, Canada) equipped with a 40 MHz RMV704 probe (VisualSonics, Canada). Tumor sizes
677 were calculated as (Length*Width*Height)/2.

678 ***Primary cell lines.*** Murine pancreatic tumors obtained from genetically engineered mouse models
679 were excised, segmented into smaller fragments, and enzymatically digested with collagenase P (0.2
680 mg/ml, Merck, Cat no. 11213857001c) and DNAse (0.5 mg/ml, Roche, Cat no. 776785) at 37°C for
681 15 minutes. This was followed by a 3 minute incubation at 37°C in 0.25% trypsin. The resulting cell
682 suspensions were cultured in RPMI 1640 medium (Cat. no. R8758), supplemented with 10% fetal
683 bovine serum and 50 units/ml penicillin-streptomycin. Epithelial clones were subsequently isolated,
684 pooled, and expanded to establish a heterogeneous cancer cell line. Human PDAC PDX-derived cell
685 cultures were prepared as previously described from patient-derived xenografts (21). The original
686 PDXs were generously provided by Dr. Manuel Hidalgo through a Material Transfer Agreement with
687 the Spanish National Cancer Centre (CNIO), Madrid, Spain (Reference no. I409181220BSMH). All
688 primary cultures underwent routine Mycoplasma testing at intervals of no more than four weeks.

689 ***PBMC isolation.*** Peripheral blood was collected in 4 ml EDTA Vacutainer tubes (BD, USA) and
690 centrifuged at 1200xg for 10 minutes at room temperature. Plasma was then collected, aliquoted and
691 stored at -80°C for future use. The remaining cell pellet was resuspended in 2 ml PBS, laid on top of
692 3 ml Ficoll-Paque (Cytiva, UK) and centrifuged at 400xg for 30 minutes with the brakes off. The PBMC
693 buffy coat was collected, washed with 2 ml PBS mixed with 1ml red blood cell lysis buffer (Invitrogen,
694 USA) and centrifuged at 260xg for 5 minutes. Additional washes with PBS were performed until the
695 supernatant was clear. Patient blood samples were obtained from the Accelerated Detection of
696 neuroEndocrine and Pancreatic TumourS (ADEPTS) biobank led by Professor Stephen Pereira.
697 Ethical approval for this study was granted by the NHS Research Ethics Committee at Queen's
698 Square, London, UK (REC reference: 06/Q0512/106). Written informed consent was provided by all
699 participants who donated samples.

700 ***Flow cytometry.*** Tumor samples underwent enzymatic digestion to produce single-cell suspensions.
701 In brief, tissues were minced using a scalpel and forceps, transferred into 50 ml conical tubes, and
702 each tube received 5 ml of serum-free medium plus 50 µl of a digestion solution consisting of
703 Collagenase P (0.2 mg/ml) and DNase (0.5 mg/ml). Samples were incubated at 37°C for 30 minutes
704 under continuous agitation. To halt digestion, 1 ml RPMI supplemented with 10% FBS was added.
705 After centrifuging at 1500 rpm for 5 minutes, supernatants were discarded. ACK buffer-mediated
706 erythrocyte lysis was carried out by incubation at room temperature for 5 minutes. Following this, cells
707 were washed in DMEM, centrifuged again, the supernatant removed, and resuspended in flow
708 cytometry buffer (PBS with 2% FBS and 3 mM EDTA).

709 For cell lines, PBS 1X washing steps preceded trypsinization with Trypsin/EDTA 0.25% (Lonza, Cat
710 no. CC-5012). Post-trypsinization, the cells were resuspended in complete RPMI medium. When
711 analyzing murine cells, cell suspensions were treated with purified anti-mouse CD16/CD32 antibodies
712 (eBioscience, Cat no. 14-9161-73) to block Fc receptor binding. Human cell preparations were
713 incubated for 15 minutes at 4°C with blocking buffer (PBS with 5% FBS and 3 mM EDTA) to reduce
714 non-specific binding.

715 Antibodies used for surface marker staining are detailed in **Supplementary Table 1**. For excluding
716 non-viable cells, samples were stained with DAPI at 2 µg/ml (4',6-diamidino-2-phenylindole; Sigma,
717 Cat no. D9542-5MG). Cells were then suspended in flow cytometry buffer [1X PBS, 3 mM EDTA (v/v)]
718 prior to analysis. Flow cytometry was performed on an Attune™ NxT Acoustic Focusing Cytometer
719 equipped with four lasers (Thermo Fisher Scientific), and data analysis was completed using FlowJo
720 software (Tree Star Inc., Ashland, OR).

721 ***Histopathology.*** For histopathological analyses, tissues were serially sectioned (3 µm thick), and
722 every 10th section was stained with hematoxylin and eosin (H&E) by the CNIO Histopathology unit.
723 Representative sections were chosen for the grading and enumeration of lesions and quantification
724 of tissue damage. For H&E-stained slides of pancreata, areas were marked as normal tissue, ADM,
725 low grade and high grade PanIN or PDAC tumor tissue. Moreover, tumors were classified as
726 differentiated or poorly differentiated using the guidelines from the College of American Pathologists
727 (https://documents.cap.org/protocols/cp-pancreas-exocrine-17protocol-4001.pdf).

728 ***Immunohistochemistry.*** Specimens were fixed in 10% formalin (Sigma) and embedded in paraffin.
729 Immunohistochemistry staining was performed by the Histopathology Unit of CNIO. For
730 histopathological analysis, specimens were serially sectioned (3 µm thick) and stained with H&E.
731 Antibodies used for mouse tissue are included in **Supplementary Table 1.** Images were analyzed
732 and exported using QuPath software (v0.5.0). For human tissue, patients have been selected from a
733 cohort already published (55). Immunohistochemistry has been performed as detailed before (56).
734 Antibodies used for human samples are included in **Supplementary Table 1**. For evaluating the
735 expression, a combined semiquantitative score was adopted, taking into account both the percentage
736 score, which is obtained based on the percentage of stained cells (score 0 = 0%, 1 = 1-25%, 2 = 26-
737 50%, 3 = 51-75%, 4 = 76-100%) and the intensity score, which is based on the intensity of the staining
738 (score 0 = no stained cells, 1 = weak staining, 2 = moderate staining, 3 = strong staining). For
739 obtaining the value of combined semiquantitative score, the value of percentage score and the value
740 of intensity score are multiplied. Thus, the combined / semiquantitative score ranges from 0 to 12.
741 The evaluation of the scores has been performed on neoplastic cells and immune cells.

742 ***Immunofluorescence and microscopy.*** Microscopy brightfield images were captured with an EVOS
743 FL Microscope (Invitrogen, Cat no. AMF4300). For immunofluorescence, FFPE sections were
744 prepared at the CNIO Histopathology unit, deparaffinized in graded ethanol, and underwent antigen
745 retrieval using 1 mM EDTA. After blocking (PBS 1x, 1% BSA, 2% FBS), primary antibodies were
746 incubated overnight at 4°C, followed by 1 hour at 37°C with secondary antibodies and DAPI. Samples
747 were mounted in ProLong (Invitrogen, Cat no. P36970) and imaged with a Confocal Stellaris 8 STED
748 microscope (Leica). Image analysis was performed using ImageJ.

749 ***RNA extraction and RT-qPCR.*** For qPCR analysis, RNA was extracted using guanidine thiocyanate
750 as described before (57) and cDNA synthesized with the SS II cDNA synthesis kit (Cat. no 18064022,
751 Invitrogen) followed by RT-qPCR analysis using SYBR green and a StepOne Plus real-time thermo-
752 cycler (Applied Biosystems). The thermal cycle consisted of an initial denaturation step of 10 min at
753 95°C followed by 40 cycles of denaturation (15 s at 95°C) and annealing (1 min at 60°C). The results
754 obtained for each gene were normalized with the β-actin levels. Primers are listed in **Supplementary**
755 **Table 2**.

756 ***Library preparation for RNA-seq***. RNA concentration was determined using a NanoDrop
757 spectrophotometer, and RNA quality was evaluated based on the RNA Integrity Number (RIN) using
758 the LabChip GX Touch Nucleic Acid Analyzer (PerkinElmer). RNA quality control, library preparation,
759 and sequencing were performed at the CNIO Genomics Unit. For library generation, 1 µg of total RNA
760 was processed using the NEBNext Ultra II Directional RNA Library Prep Kit for Illumina (NEB #E7760),
761 following the manufacturer's recommendations. Briefly, the poly(A)+ RNA fraction was isolated and
762 fragmented, followed by synthesis of double-stranded cDNA. Subsequent enzymatic steps included
763 end-repair, dA-tailing, and adapter ligation. The adapter-ligated products were amplified by PCR using
764 Illumina paired-end primers. Final libraries were loaded onto an Illumina flow cell for cluster generation
765 and sequenced on an Illumina NextSeq 500 system according to the manufacturer's protocol.

766 **DNA extraction and Illumina Mouse Methylation microarrays.** Genomic DNA was extracted at the
767 Genomics Unit of the Josep Carreras Leukemia Research Institute. Briefly, DNA was isolated from
768 cell pellets using the DNeasy Blood & Tissue Kit (Qiagen, Hilden, Germany) and quantified with a

769 Qubit fluorometer. DNA integrity was assessed by agarose gel electrophoresis, and samples (≥600
770 ng per sample) were bisulfite-converted using the EZ-96 DNA Methylation Kit (Zymo Research Corp.,
771 CA, USA) according to the manufacturer's instructions. Bisulfite-converted DNA was then hybridized
772 to Infinium Mouse Methylation microarrays as previously described by García-Prieto *et al.* (58).

773 **Endoscopic ultrasound database generation.** Upon approval from the Internal Review Board (IRB
774 BIO-PANCREAS, version 3, 2021), specimens were collected from patients diagnosed with
775 pancreatic ductal adenocarcinoma (PDAC) at San Raffaele Research Hospital. Eligible subjects
776 included treatment-naïve individuals with clinical histories and radiological findings indicative of
777 PDAC. Patients were not involved in the design, implementation, analysis, or dissemination of the
778 study. Informed consent was obtained prior to conducting diagnostic EUS procedures under deep
779 intravenous sedation with Propofol (Diprivan, Zeneca, Germany). Procedures utilized a Pentax
780 therapeutic linear echoendoscope (EG3870UTK, EG38J10UT) in conjunction with Hitachi ultrasound
781 systems (Arietta 850, Arietta V70). EUS-guided tissue acquisition (TA) was performed using a 25G
782 fine-needle aspiration (FNA) needle (Expect Slimline, Boston Scientific) employing the slow-pull
783 technique. RNA was subsequently isolated, quantified, and evaluated according to established
784 protocols (17).

785 ***RNA-sequencing analysis.*** FASTQ file integrity was verified using MD5 checksum comparison, and
786 read quality was assessed with FastQC, with optional contamination screening via FastQ Screen; all
787 quality metrics were summarized in a MultiQC report. Reads from different lanes were concatenated,
788 optionally downsampled to a fixed number of reads using a defined seed and trimmed for adapters
789 and low-quality bases using bbduk (BBTools). Reads were then aligned using STAR, HISAT2, or
790 Salmon as specified in the configuration; STAR and HISAT2 used genome indices generated from a
791 reference FASTA and GTF annotation (with HISAT2 outputs subsequently sorted using samtools),
792 while Salmon performed pseudo-alignment using a transcriptome-based index. For STAR and
793 HISAT2 alignments, gene-level quantification was performed with htseq-count or featureCounts after
794 indexing BAM files with samtools, using the same GTF annotation employed for alignment.
795 Per-sample count files were merged into a final counts matrix for downstream differential expression

796 analysis. Differentially expressed genes (DEGs) were identified from count matrices using DESeq2 in
797 R, excluding genes with fewer than five counts. The Wald test was employed to determine significant
798 changes in expression between conditions, while Principal Component Analysis (PCA) was used to
799 evaluate variability among samples. DEGs for each condition were selected considering Log2FC ≠ 0
800 and p ≤0.05 and subsequently ranked according to their Log2FC value. Gene set enrichment analysis
801 (GSEA) was performed using annotations from Reactome, KEGG, and MSigDB
802 (www.broadinstitute.org/gsea/index.jsp), as well as custom gene sets described in **Supplementary**
803 **Table 3**. In addition, genes were ranked using moderated t statistics from limma. After applying the
804 Kolmogorov-Smirnov test, gene sets with FDR < 0.25 were considered significantly enriched.

805 For the EUS dataset, we performed two kinds of analyses. For the differentially expressed genes in
806 patients with body mass index (BMI) <25 or ≥25, we employed limma package (R/Bioconductor). A
807 design matrix was constructed including BMI group as the primary variable of interest and adjusting
808 for relevant covariates (sex, age, smoking status, batch, and RNA extraction methodology). Linear
809 models were fitted to the expression matrix using lmFit, followed by empirical Bayes moderation with
810 eBayes. Differentially expressed genes for the *Obese vs. reference BMI group* contrast were
811 extracted using topTable. To assess global transcriptional patterns and sample structure, a principal
812 component analysis (PCA) was conducted, and samples were visualized according to BMI group.
813 Differential expression results were further summarized using a volcano plot highlighting genes with
814 nominal $p < 0.05$. Significant genes were filtered based on nominal significance and exported with
815 their log fold changes, *p*-values, and adjusted *p*-values for downstream interpretation. For a set of
816 predefined stem-related genes, we generated violin plots to visualize their expression distribution
817 across BMI groups. For each gene present in the expression matrix, a sample-level dataset was
818 constructed by pairing log-RPKM expression values with the corresponding BMI group. Violin plots
819 were generated using ggplot2, combining kernel density estimates with overlaid boxplots to
820 summarize central tendency and dispersion. Group differences in gene expression were statistically
821 evaluated using the Wilcoxon rank-sum test, and the resulting *p*-values were annotated directly on
822 each plot.

823 For the organoid implantation assay dataset (GSE148135), Raw counts were normalized and
824 converted in logCPM using edgeR (R package). For the figure, the p values refer to Dunn_test that
825 was used post Kruskall-Wallis to test difference in expression.

826 For the PBMC RNA-seq, RNA was extracted from isolated PBMC samples using the RNeasy Mini Kit
827 (Qiagen, Germany), according to the manufacturer's recommendations. RNA concentration and
828 integrity were measured using a NanoDrop™ 2000 Spectrophotometer (ThermoFisher, UK) and
829 TapeStation RNA High sensitivity assay (Agilent, USA), respectively. In collaboration with UCL
830 Genomics (UCLG), cDNA libraries were prepared using the Watchmaker RNA Library Prep Kit with
831 Polaris rRNA and Globin Depletion (Watchmaker Genomics, USA). Libraries were indexed using IDT
832 xGen unique dual index (UDI) adapters incorporating unique molecular identifiers (UMIs) and
833 sequenced with the NovaSeq 6000 (S4 v1.5 flow cell, 300 cycles, XP workflow), to generate paired-
834 end 150 bp reads, yielding approximately 40 million read pairs per sample. Demultiplexing, quality
835 control (FastQC and MultiQC), and transcript quantification using Salmon (pseudo-mapping) were
836 performed by UCLG to generate gene-level raw count matrices for downstream analysis. Data
837 normalisation and differential gene expression analysis were conducted using DESeq2 via the
838 SARTools package, developed by Hugo Varet *et al.* (59), and analysis quality was assessed using
839 principal component analysis (PCA) and additional diagnostic visualisations. Significantly differentially
840 expressed genes were identified as those with an adjusted p value <0.05 and log2 fold-change<1
841 between comparison groups.

842 **DNA methylation analysis.** Raw signal intensity files (IDATs) were processed using standard settings
843 in the SeSAMe R package. Unsupervised analyses of the global methylome were performed using t-
844 SNE. Supervised analyses were conducted by calculating mean methylation values per condition and
845 per CpG site, and CpG sites with absolute methylation differences between conditions ≥0.33 were
846 considered biologically meaningful. Differential methylation was assessed using a linear regression
847 model implemented in the limma R package, and CpG sites with an adjusted P-value ≤0.05 were
848 considered significant. CpG sites were annotated using the annotation described in García-Prieto *et*
849 *al*., and downstream analyses included gene set enrichment analysis of gene-associated CpG sites

using the EnrichR R package (ref) and the Panther database. Pathways were considered significant if they had adjusted P-values ≤0.05.

hCAP-18/LL-37 ELISA. Patients with suspected or confirmed pancreatic ductal adenocarcinoma (PDAC) were recruited from the General Surgery, Gastroenterology, and Medical Oncology departments of Ramón y Cajal University Hospital (Madrid, Spain). The study was approved by the local ethics committee, and all participants provided written informed consent. Blood samples were collected at study entry, prior to any oncological treatment, for serum isolation. Serum samples from healthy individuals without a history of digestive disease or cancer were obtained from the Ramón y Cajal–IRYCIS Biobank (PT20/0045; PT23/00098), part of the Spanish National Biobanks Network (ISCIII Biobank Register No. B.0000678). Serum LL-37 levels were quantified using a commercial ELISA kit (ELabScience, E-EL-H2438) according to the manufacturer's instructions. Samples were diluted 1:10 and incubated on plates pre-coated with LL-37-specific capture antibodies. Following incubation with detection antibodies and chromogenic substrate, absorbance was measured at 450 nm with correction at 540 nm. Concentrations were calculated by interpolation from a standard curve and expressed as ng/mL. All samples were analyzed in duplicate, and those with intra-assay coefficients of variation >15% were excluded.

Macrophage isolation. Murine bone marrow-derived cells (BMDCs) were harvested from the femurs and tibiae of a minimum of three mice using centrifugation. The resulting BMDC pellets were resuspended in RPMI 1640 medium (Invitrogen, Cat. No. 61870044) and incubated for 24 h to facilitate monocyte attachment. Subsequently, monocytes were differentiated into macrophages under adherent conditions for 5-7 days on non-tissue culture-treated 100 mm dishes in RPMI supplemented with 10% FBS and 10 ng/ml murine M-CSF (PeproTech, Cat. No. 315-02). Additionally, certain experiments utilized immortalized murine bone marrow-derived macrophages generously provided by Dr. Antonio Castrillo.

Macrophage conditioning and co-culture assays. After differentiation, for macrophage polarization, they were cultured without stimulation to obtain untrained conditioned medium or with stimulation (fatty acids) for 24 h to obtain a lipid loaded state. Then, polarization medium was removed

877 and RPMI was left to be conditioned for 48 h to obtain fatty acid trained-macrophage conditioned
878 medium.

879 ***Phagocytosis assay.*** Five days after isolation of macrophages, tumor fluorescent cells were
880 harvested and seeded together with macrophages during 24 h. Afterwards, cells were detached using
881 scrapers and macrophages phagocytosing fluorescent tumor cells were measured by flow cytometry,
882 as described above, gating on the double-positive population: F4/80 and reporter genes (i.e., YFP).

883 ***Stimulation assays.*** For stimulation assays, tumor or immune cells were seeded in 6-well plates and
884 treated with 1 ml of complete RPMI medium plus recombinant CAMP (5 µg/mL, Cat. no. HY-P4855,
885 MedChemExpress) during 24h/48h, fatty acids (50 µM, oleic acid; 50 µM sodium palmitate; 200 µM
886 linoleic acid; Cat no. O3008, P9767, L9530) or MØ-derived conditioned media. After indicated time
887 points, cells were trypsinized or scraped and harvested for flow cytometry of the indicated markers or
888 RNA-seq analysis.

889 ***Spheroid formation assay.*** Cancer stem cell-enriched spheroids were cultured employing 2000 cells
890 per well in ultra-low attachment plates (Corning) during 4-7 days using serum-free DMEM/F12
891 medium (Invitrogen, Cat no. 21331046) with B27 (1:50; Invitrogen, Cat no. 17504044), 20 ng/ml bFGF
892 (PAN-Biotech, Sigma, Cat no. GF446-10UG), L-Glutamine (Invitrogen, Cat no. 25030081) and 50
893 units/ml penicillin-streptomycin (Invitrogen, Cat no. 11548876).

894 ***Transwell invasion assay.*** Cell invasion assays were performed using 24-well Transwell chambers
895 (Corning, NY) equipped with polycarbonate inserts containing 8 µm pores. Inserts were coated with
896 50 µL of Matrigel (Corning, NY) diluted 1:3 in culture medium. A total of 50000 cells suspended in
897 serum-free medium were seeded into the upper chambers, while the lower wells were filled with
898 medium containing 1% FBS as a chemoattractant. After 24 h of incubation, non-invading cells on the
899 upper surface of the membrane were gently removed with a cotton swab. Cells that had migrated to
900 the lower membrane surface were fixed with 0.1% glutaraldehyde, stained with 0.5% crystal violet,
901 and visualized under a light microscope. The number of invaded cells was quantified by counting five
902 randomly selected microscopic fields.

903 ***Wound healing assay.*** Cells were seeded (100000) into 24-well plates and grown until reaching
904 approximately 95% of confluent monolayers. A straight line was scratched through the monolayer with
905 a 10 µL pipette tip to create a wound. Then, the closure of the wound was visualized using an EVOS
906 phase-contrast microscopy and the gap distance between the edges was calculated using ImageJ
907 software.

908 ***Statistical analysis.*** Results are reported as means ± standard error of the mean (SEM) or standard
909 deviation (STDEV), as specified. Differences between group means were assessed using Student's
910 t-test, unless otherwise indicated in the figure legends. P values less than 0.05 were deemed
911 statistically significant, while non-significant outcomes are denoted as "ns". All statistical analyses
912 were conducted using GraphPad Prism version 8.0 (San Diego, California, USA).

913 **RESOURCE AVAILABILITY**

914 **Lead contact**

915 Requests for further information and resources of this study should be directed to the lead contact,
916 Dr. Carmen Guerra (mcguerra@cnio.es).

917 **Materials availability**

918 All data related to the results are available as part of the article. Additional information will be available
919 on request.

920 **Data and code availability**

921 Unique identifiers for publicly available datasets are indicated, a list of figures that have associated
922 raw data can be provided, and there are no restrictions on data availability. Data from the EUS dataset
923 can be provided upon reasonable request and DTA signing with the San Raffaele Hospital. This paper
924 does not report any original code. Further information if required is available from the lead contact
925 upon request.

926

927 **ACKNOWLEDGEMENTS**

928 We thank the patients and healthy controls for donating samples. We especially thank the help of
929 Marta San Roman, María del Carmen Lechuga, Alejandra López, and Raquel Villar from the CNIO
930 Experimental Oncology group. We also want to thank the Isabel Aragón from the CNIO Animal Facility,
931 IIBm Microscopy Unit, CNIO Confocal Microscopy Unit, CNIO and IJC Genomics Unit and the CNIO
932 Histopathology Unit for their support. A.G.-d-R. was supported by an AECC Predoctoral Fellowship
933 (PRDMA246123GALV) and J.C.L-G. was supported by a "CNIO Friends" Postdoctoral Fellowship and
934 an AECC Postdoctoral Fellowship (POSTD258037LÓPE). E.Z.-D. and P.S. were supported by
935 "Formación de Personal Investigador" (FPI) fellowship (PRE2022- 102952) from the Spanish Ministry
936 of Sciences and Innovation and by a fellowship from the China Scholarship Council respectively. This
937 work has been supported by the IX Carmen Delgado/Miguel Pérez-Mateo grant (C.G.), a CRIS
938 Cancer Foundation grant, European Research Council (ERC-AG/695566-THERACAN), CIBERONC
939 Fund (CB21/12/00121), and the Agencia Estatal de Investigación cofounded with the European
940 Regional Development Fund, 'A way to make Europe' project PID2024-160242NB-I00 (C.G., M.B.).
941 Also, this work has received support from the Cancer Research Institute (New York, NY, USA,
942 B.S.,Jr.), the AECC with a LAB AECC grant (LABAE223389SANC, to P.S.), the AIRC (IG 26201, G.C.;
943 AIRC IG 32351, C.C.; MBe is supported by AIRC fellowships, 28054, 29829), the PNRR Program
944 (code PNRR-MCNT2-2023-12377229, CUP C53C23001140007) and NEXTGENERATION-EU
945 Project "ICSC" SPOKE8 (CN00000013, CUP J33C22001180001) (both C.C.; PRIN 2022, code:
946 2022CMMRWA, CUP: B53D23008010006, C.L.), Fondazione Italiana Malattie Pancreas (FIMP-
947 Ministero Salute J38D19000690001, C.L.), and the European Regional Development Fund, 'A way to
948 make Europe' ERDF project PID2024-159192OB-I00 (M.E.) and PID2024-157515OB-I00 (B.S.,Jr.).
949 S.P.P. and P.A. are funded by Cancer Research UK (grant C12077/A26223) and Pancreatic Cancer
950 UK, with patient serum samples provided through the PCUK ADEPTS study (REC reference:
951 06/Q0512/106). S.P.P. is also supported by the National Institute for Health and Care Research
952 University College London Hospitals Biomedical Research Centre. We also want to thank Dr.
953 Mercedes Rodriguez Garrote, Marta Pardo, and Biobank and Biomodels Platform (PT20/0045;

PT23/00098), ISCIII research and development platforms in biomedicine and health sciences for supplying the clinical samples and data, as well as the UCL Genomics (UCLG), Zayed Centre for Research into Rare Disease in Children, London, UK (Research Resource Unique Identifier: RRID:SCR_027010) for help with the PBMC RNA-seq dataset. This work has also been developed upon work from COST Action “Identification of biological markers for prevention and translational medicine in pancreatic cancer (TRANSPAN),” CA21116, supported by COST (European Cooperation in Science and Technology).

Finally, we would like to thank the other current and past members of the CNIO Experimental Oncology group and the Cancer Stem Cells and Fibroinflammatory Microenvironment group for helpful discussions, technical assistance and support, as well as María del Castillo and Marta Hergueta from the CNIO Microenvironment and Metastasis group, and Jaime Martínez from CNIO Epithelial Carcinogenesis group.

AUTHOR CONTRIBUTIONS

Conceptualization of the study: C.G. and M.B. *In vitro* experimental work: A.G.-d-R., J.C.L.-G., S.A., J.E., B.P.-A., A.R., P.Sun. *In vivo* experimental work: A.G.-d-R., J.C.L.-G., P.Sun., E.Z.-D., B.R.-P., R.B., S.J.-P. Bioinformatic analyses: A.G.-d-R., J.C.L.-G., A.A., A.N., K.F. Mouse pathology analyses: A.G.-d-R., J.C.L.-G., C.G. Human pathology analyses: M.Be., C.L. Human transcriptomic data from patients: L.A., G.C. Formal analyses and investigation were made by A.G.-d-R., J.C.L.-G. Resources were provided by B.S.Jr., C.G., M.B. The original draft was written by A.G.-d-R. and J.C.L.-G. All authors contributed reviewing and editing the manuscript. C.G. and M.B supervised the development of the project. P.S., G.C., M.E., S.P.P., P.A., C.C., B.S.Jr., C.G. and M.B. obtained the funding involved in the development of the study.

REFERENCES

1. The global, regional, and national burden of pancreatic cancer and its attributable risk factors in 195 countries and territories, 1990-2017: a systematic analysis for the Global Burden of Disease Study 2017. The lancet Gastroenterology & hepatology. 2019;4(12):934-47.
2. Cancer.net. Pancreatic Cancer: Statistics Cancer.net: ASCO; 2022 [updated 02/2022. Available from: https://www.cancer.net/cancer-types/pancreatic-cancer/statistics#:~:text=The%20general%205%2Dyear%20survival,disease%20when%20it%20is%20diagnosed.
3. Luo D, Li Y, Yu X, Ji L, Gong X. Early onset pancreatic cancer: A review. Translational oncology. 2025;52:102239.
4. Carpenter ES, Elhossiny AM, Kadiyala P, Li J, McGue J, Griffith BD, et al. Analysis of Donor Pancreata Defines the Transcriptomic Signature and Microenvironment of Early Neoplastic Lesions. Cancer discovery. 2023;13(6):1324-45.
5. Guerra C, Collado M, Navas C, Schuhmacher AJ, Hernández-Porras I, Cañamero M, et al. Pancreatitis-induced inflammation contributes to pancreatic cancer by inhibiting oncogene-induced senescence. Cancer Cell. 2011;19(6):728-39.
6. Guerra C, Schuhmacher AJ, Cañamero M, Grippo PJ, Verdaguer L, Pérez-Gallego L, et al. Chronic Pancreatitis Is Essential for Induction of Pancreatic Ductal Adenocarcinoma by K-Ras Oncogenes in Adult Mice. Cancer Cell. 2007;11(3):291-302.
7. Salvador-Barbero B, Alatsatianos M, Morton JP, Sansom OJ, Hogan C. KRASG12D Cells Override Homeostatic Cell Elimination Mechanisms in Adult Pancreas Via Wnt5a and Cell Dormancy. Gastroenterology. 2025.
8. López-Gil JC, García-Silva S, Ruiz-Cañas L, Navarro D, Palencia-Campos A, Giráldez-Trujillo A, et al. The Peptidoglycan Recognition Protein 1 confers immune evasive properties on pancreatic cancer stem cells. Gut. 2024:gutjnl-2023-330995.
9. Incio J, Liu H, Suboj P, Chin SM, Chen IX, Pinter M, et al. Obesity-Induced Inflammation and Desmoplasia Promote Pancreatic Cancer Progression and Resistance to Chemotherapy. Cancer discovery. 2016;6(8):852-69.
10. Philip B, Roland CL, Daniluk J, Liu Y, Chatterjee D, Gomez SB, et al. A high-fat diet activates oncogenic Kras and COX2 to induce development of pancreatic ductal adenocarcinoma in mice. Gastroenterology. 2013;145(6):1449-58.
11. Song SH, Jeon MS, Nam JW, Kang JK, Lee YJ, Kang JY, et al. Aberrant GATA2 epigenetic dysregulation induces a GATA2/GATA6 switch in human gastric cancer. Oncogene. 2018;37(8):993-1004.
12. Martinelli P, Carrillo-de Santa Pau E, Cox T, Sainz B, Jr., Dusetti N, Greenhalf W, et al. GATA6 regulates EMT and tumour dissemination, and is a marker of response to adjuvant chemotherapy in pancreatic cancer. Gut. 2017;66(9):1665-76.
13. Youssef KK, Narwade N, Arcas A, Marquez-Galera A, Jiménez-Castaño R, Lopez-Blau C, et al. Two distinct epithelial-to-mesenchymal transition programs control invasion and inflammation in segregated tumor cell populations. Nature Cancer. 2024;5(11):1660-80.
14. Sainz B, Jr., Martín B, Tatari M, Heeschen C, Guerra S. ISG15 Is a Critical Microenvironmental Factor for Pancreatic Cancer Stem Cells. Cancer Research. 2014;74(24):7309-20.
15. Jiang Z, Wu F, Laise P, Takayuki T, Na F, Kim W, et al. Tff2 defines transit-amplifying pancreatic acinar progenitors that lack regenerative potential and are protective against Kras-driven carcinogenesis. Cell Stem Cell. 2023;30(8):1091-109.e7.
16. Leinenkugel G, Kong B, Raulefs S, Miller K, Roth S, Jiang H, et al. Sca-1 is a marker for cell plasticity in murine pancreatic epithelial cells and induced by IFN-β in vitro. Pancreatology. 2022;22(2):294-303.
17. Valle S, Alcalá S, Martin-Hijano L, Cabezas-Sáinz P, Navarro D, Muñoz ER, et al. Exploiting oxidative phosphorylation to promote the stem and immunoevasive properties of pancreatic cancer stem cells. Nature Communications. 2020;11(1):5265.

18. Westphalen CB, Takemoto Y, Tanaka T, Macchini M, Jiang Z, Renz BW, et al. Dclk1 Defines Quiescent Pancreatic Progenitors that Promote Injury-Induced Regeneration and Tumorigenesis. Cell Stem Cell. 2016;18(4):441-55.
19. Sainz B, Alcala S, Garcia E, Sanchez-Ripoll Y, Azevedo MM, Cioffi M, et al. Microenvironmental hCAP-18/LL-37 promotes pancreatic ductal adenocarcinoma by activating its cancer stem cell compartment. Gut. 2015;64(12):1921-35.
20. Cioffi M, Trabulo S, Hidalgo M, Costello E, Greenhalf W, Erkan M, et al. Inhibition of CD47 Effectively Targets Pancreatic Cancer Stem Cells via Dual Mechanisms. Clinical Cancer Research. 2015;21(10):2325-37.
21. Bailey JM, Alsina J, Rasheed ZA, McAllister FM, Fu YY, Plentz R, et al. DCLK1 marks a morphologically distinct subpopulation of cells with stem cell properties in preinvasive pancreatic cancer. Gastroenterology. 2014;146(1):245-56.
22. Li C, Wu JJ, Hynes M, Dosch J, Sarkar B, Welling TH, et al. c-Met is a marker of pancreatic cancer stem cells and therapeutic target. Gastroenterology. 2011;141(6):2218-27.e5.
23. Dumartin L, Alrawashdeh W, Trabulo SM, Radon TP, Steiger K, Feakins RM, et al. ER stress protein AGR2 precedes and is involved in the regulation of pancreatic cancer initiation. Oncogene. 2017;36(22):3094-103.
24. Rovira M, Scott SG, Liss AS, Jensen J, Thayer SP, Leach SD. Isolation and characterization of centroacinar/terminal ductal progenitor cells in adult mouse pancreas. Proc Natl Acad Sci U S A. 2010;107(1):75-80.
25. Parejo-Alonso B, Barneda D, Trabulo SMD, Courtois S, Compte-Sancerni S, Zurkovic J, et al. PPAR-δ Orchestrates a Pro-metastatic Metabolic Response to Microenvironmental Cues in Pancreatic Cancer. Cancer Research. 2025.
26. Parejo-Alonso B, Royo-García A, Espiau-Romera P, Courtois S, Curiel-García Á, Zagorac S, et al. Pharmacological targeting of the receptor ALK inhibits tumorigenicity and overcomes chemoresistance in pancreatic ductal adenocarcinoma. Biomedicine & pharmacotherapy = Biomedecine & pharmacotherapie. 2023;158:114162.
27. Archibugi L, Ruta V, Panzeri V, Redegalli M, Testoni SGG, Petrone MC, et al. RNA Extraction from Endoscopic Ultrasound-Acquired Tissue of Pancreatic Cancer Is Feasible and Allows Investigation of Molecular Features. Cells. 2020;9(12).
28. Lupo F, Piro G, Torroni L, Delfino P, Trovato R, Rusev B, et al. Organoid-Transplant Model Systems to Study the Effects of Obesity on the Pancreatic Carcinogenesis in vivo. Frontiers in cell and developmental biology. 2020;8:308.
29. Hermann PC, Huber SL, Herrler T, Aicher A, Ellwart JW, Guba M, et al. Distinct Populations of Cancer Stem Cells Determine Tumor Growth and Metastatic Activity in Human Pancreatic Cancer. Cell Stem Cell. 2007;1(3):313-23.
30. Wang Z, Kim SY, Tu W, Kim J, Xu A, Yang YM, et al. Extracellular vesicles in fatty liver promote a metastatic tumor microenvironment. Cell metabolism. 2023;35(7):1209-26.e13.
31. Liu X, Song J, Yuan M, Zuo F, Li H, Tang L, et al. Single-cell transcriptional dissection illuminates an evolution of immunosuppressive microenvironment during pancreatic ductal adenocarcinoma metastasis. Signal transduction and targeted therapy. 2025;10(1):182.
32. Mascaraque M, Courtois S, Royo-García A, Barneda D, Stoian AM, Villaoslada I, et al. Fatty acid oxidation is critical for the tumorigenic potential and chemoresistance of pancreatic cancer stem cells. Journal of translational medicine. 2024;22(1):797.
33. Hoang-Yen Tran D, Hoang-Ngoc Tran D, Mattai SA, Sallam T, Ortiz C, Lee EC, et al. Cathelicidin suppresses lipid accumulation and hepatic steatosis by inhibition of the CD36 receptor. International journal of obesity (2005). 2016;40(9):1424-34.
34. Popa AD, Gherasim A, Caba L, Niță O, Graur M, Mihalache L, et al. Cathelicidin: Insights into Its Impact on Metabolic Syndrome and Chronic Inflammation. Metabolites. 2024;14(12).
35. Hingorani SR, Wang L, Multani AS, Combs C, Deramaudt TB, Hruban RH, et al. Trp53R172H and KrasG12D cooperate to promote chromosomal instability and widely metastatic pancreatic ductal adenocarcinoma in mice. Cancer Cell. 2005;7(5):469-83.
36. Hosoda W, Chianchiano P, Griffin JF, Pittman ME, Brosens LAA, Noë M, et al. Genetic analyses of isolated high-grade pancreatic intraepithelial neoplasia (HG-PanIN) reveal paucity of alterations in TP53 and SMAD4. The Journal of Pathology. 2017;242(1):16-23.

37. Matsuda Y, Furukawa T, Yachida S, Nishimura M, Seki A, Nonaka K, et al. The Prevalence and Clinicopathological Characteristics of High-Grade Pancreatic Intraepithelial Neoplasia: Autopsy Study Evaluating the Entire Pancreatic Parenchyma. Pancreas. 2017;46(5):658-64.
38. Longnecker DS, Suriawinata AA. Incidence of Pancreatic Intraepithelial Neoplasia in an Autopsy Series. Pancreas. 2022;51(4):305-9.
39. Burdziak C, Alonso-Curbelo D, Walle T, Reyes J, Barriga FM, Haviv D, et al. Epigenetic plasticity cooperates with cell-cell interactions to direct pancreatic tumorigenesis. Science. 2023;380(6645):eadd5327.
40. Alonso-Curbelo D, Ho YJ, Burdziak C, Maag JLV, Morris JPt, Chandwani R, et al. A gene-environment-induced epigenetic program initiates tumorigenesis. Nature. 2021;590(7847):642-8.
41. Caronni N, La Terza F, Vittoria FM, Barbiera G, Mezzanzanica L, Cuzzola V, et al. IL-1β(+) macrophages fuel pathogenic inflammation in pancreatic cancer. Nature. 2023;623(7986):415-22.
42. Tu M, Klein L, Espinet E, Georgomanolis T, Wegwitz F, Li X, et al. TNF-α-producing macrophages determine subtype identity and prognosis via AP1 enhancer reprogramming in pancreatic cancer. Nature Cancer. 2021;2(11):1185-203.
43. Ma Z, Lytle NK, Chen B, Jyotsana N, Novak SW, Cho CJ, et al. Single-Cell Transcriptomics Reveals a Conserved Metaplasia Program in Pancreatic Injury. Gastroenterology. 2022;162(2):604-20.e20.
44. Storz P. Acinar cell plasticity and development of pancreatic ductal adenocarcinoma. Nature reviews Gastroenterology & hepatology. 2017;14(5):296-304.
45. Pinho AV, Rooman I, Reichert M, De Medts N, Bouwens L, Rustgi AK, et al. Adult pancreatic acinar cells dedifferentiate to an embryonic progenitor phenotype with concomitant activation of a senescence programme that is present in chronic pancreatitis. Gut. 2011;60(7):958.
46. Papargyriou A, Najajreh M, Cook DP, Maurer CH, Bärthel S, Messal HA, et al. Heterogeneity-driven phenotypic plasticity and treatment response in branched-organoid models of pancreatic ductal adenocarcinoma. Nat Biomed Eng. 2025;9(6):836-64.
47. Benitz S, Steep A, Nasser MM, Preall J, Mahajan UM, McQuithey H, et al. ROR2 Regulates Cellular Plasticity in Pancreatic Neoplasia and Adenocarcinoma. Cancer discovery. 2024;14(11):2162-82.
48. Pitter KL, Grbovic-Huezo O, Joost S, Singhal A, Blum M, Wu K, et al. Systematic Comparison of Pancreatic Ductal Adenocarcinoma Models Identifies a Conserved Highly Plastic Basal Cell State. Cancer Res. 2022;82(19):3549-60.
49. Espinet E, Klein L, Puré E, Singh SK. Mechanisms of PDAC subtype heterogeneity and therapy response. Trends in cancer. 2022;8(12):1060-71.
50. Pegoraro A, De Marchi E, Ferracin M, Orioli E, Zanoni M, Bassi C, et al. P2X7 promotes metastatic spreading and triggers release of miRNA-containing exosomes and microvesicles from melanoma cells. Cell Death & Disease. 2021;12(12):1088.
51. Qiu Y, Li W-h, Zhang H-q, Liu Y, Tian X-X, Fang W-G. P2X7 Mediates ATP-Driven Invasiveness in Prostate Cancer Cells. PloS one. 2014;9(12):e114371.
52. Wang J, Cheng M, Law IKM, Ortiz C, Sun M, Koon HW. Cathelicidin Suppresses Colon Cancer Metastasis via a P2RX7-Dependent Mechanism. Molecular Therapy - Oncolytics. 2019;12:195-203.
53. Guerra C, Mijimolle N, Dhawahir A, Dubus P, Barradas M, Serrano M, et al. Tumor induction by an endogenous K-ras oncogene is highly dependent on cellular context. Cancer Cell. 2003;4(2):111-20.
54. Jonkers J, Meuwissen R, van der Gulden H, Peterse H, van der Valk M, Berns A. Synergistic tumor suppressor activity of BRCA2 and p53 in a conditional mouse model for breast cancer. Nature genetics. 2001;29(4):418-25.
55. Luchini C, Franzina C, Caldart F, De Pretis N, Crestani M, Donadelli M, et al. Fatty Pancreas Disease: An Integrated Study on Frozen Tissues Shows Distinct Compartments of Interlobular/Intralobular, Intra-Acinar, and Intra-Islet Fat Deposition. Laboratory investigation; a journal of technical methods and pathology. 2025;105(11):104214.
56. Pea A, Bevere M, Gkountakos A, Pasini D, Fiorini D, Mafficini A, et al. Mucinous cystic neoplasms and simple mucinous cysts are two distinct precursors of pancreatic cancer: clinicopathological, genomic, and transcriptomic characterization. J Pathol. 2025;266(4-5):421-34.

57. Chomczynski P, Sacchi N. Single-step method of RNA isolation by acid guanidinium thiocyanate-phenol-chloroform extraction. Analytical biochemistry. 1987;162(1):156-9.
58. Garcia-Prieto CA, Álvarez-Errico D, Musulen E, Bueno-Costa A, B NV, Vaquero A, et al. Validation of a DNA methylation microarray for 285,000 CpG sites in the mouse genome. Epigenetics. 2022;17(12):1677-85.
59. Varet H, Brillet-Guéguen L, Coppée J-Y, Dillies M-A. SARTools: A DESeq2- and EdgeR-Based R Pipeline for Comprehensive Differential Analysis of RNA-Seq Data. PloS one. 2016;11(6):e0157022.

1149 # SUPPLEMENTARY FIGURES

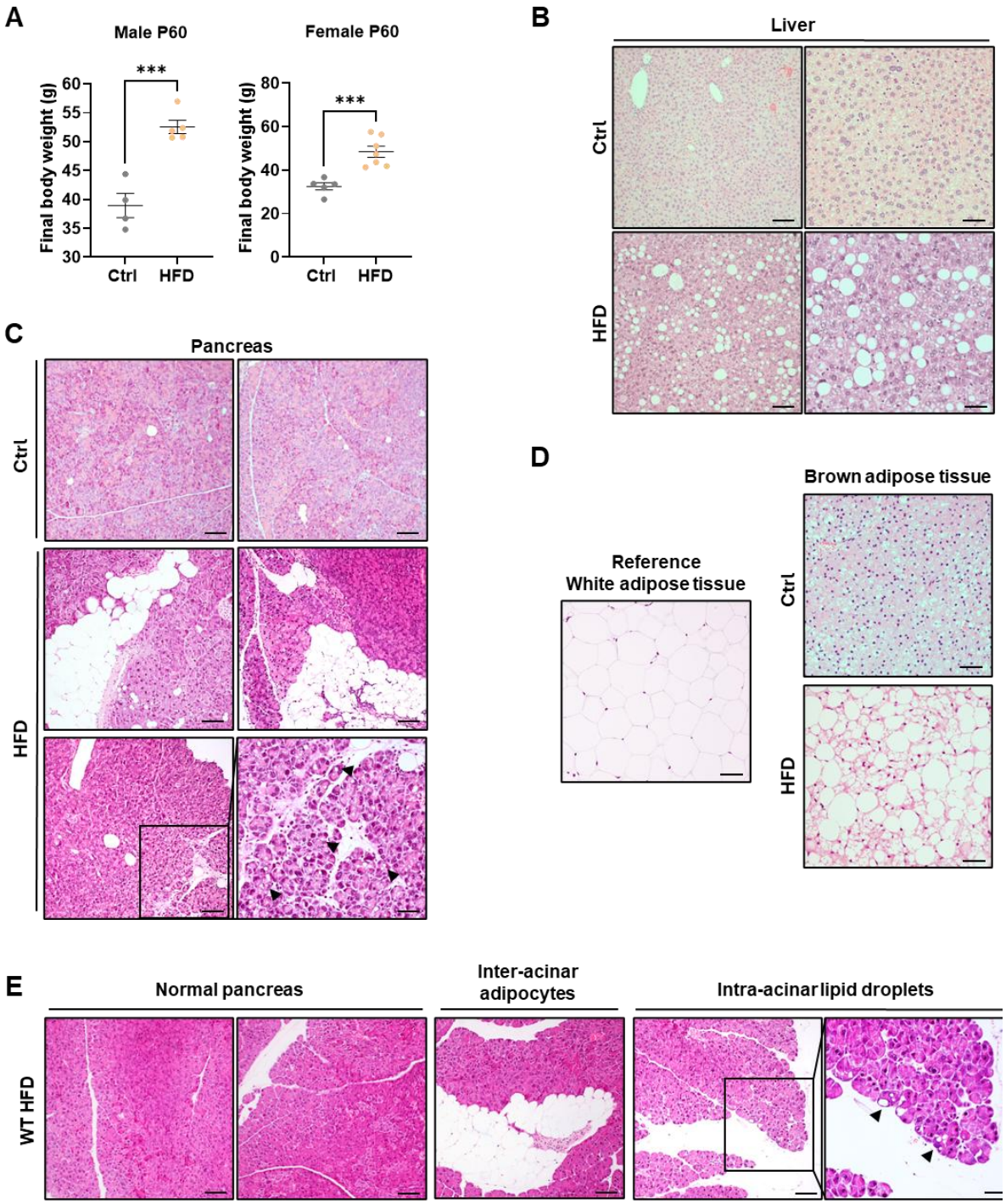

1150

1151 ***Figure S1. High-fat diet induces obesity traits in murine models. A)*** *Quantification of final weight from*
1152 *control (Ctrl) and high-fat diet (HFD) exposed mice included in the P60 protocol divided by sex (males, left*
1153 *panel; females, right panel), shown as the mean ± SEM (n=4 Ctrl males, 5 HFD males, 5 Ctrl females, 7 HFD*
1154 *females, P values as determined by unpaired T-test).* ***B)*** *Representative brightfield microscopy images of H&E*
1155 *staining from the liver from Ctrl and HFD exposed mice.* ***C)*** *Representative brightfield microscopy images of*
1156 *H&E staining from the pancreata from Ctrl and HFD exposed mice. Scale bar=100 µm (left column), 50 µm*
1157 *(right column). Black arrowheads point out intra-acinar lipid droplets observed in HFD-fed mice.* ***D)***
1158 *Representative brightfield microscopy images of H&E staining from the white (as a reference) and brown*

1159 *adipose tissue from Ctrl and HFD exposed mice.* ***E)*** *Representative brightfield microscopy images of H&E*
1160 *staining from the pancreata from C57Bl/6 mice exposed to HFD. Black arrowheads point out intra-acinar lipid*
1161 *droplets. Scale bar=100 µm, 50 µm (picture in the right).*

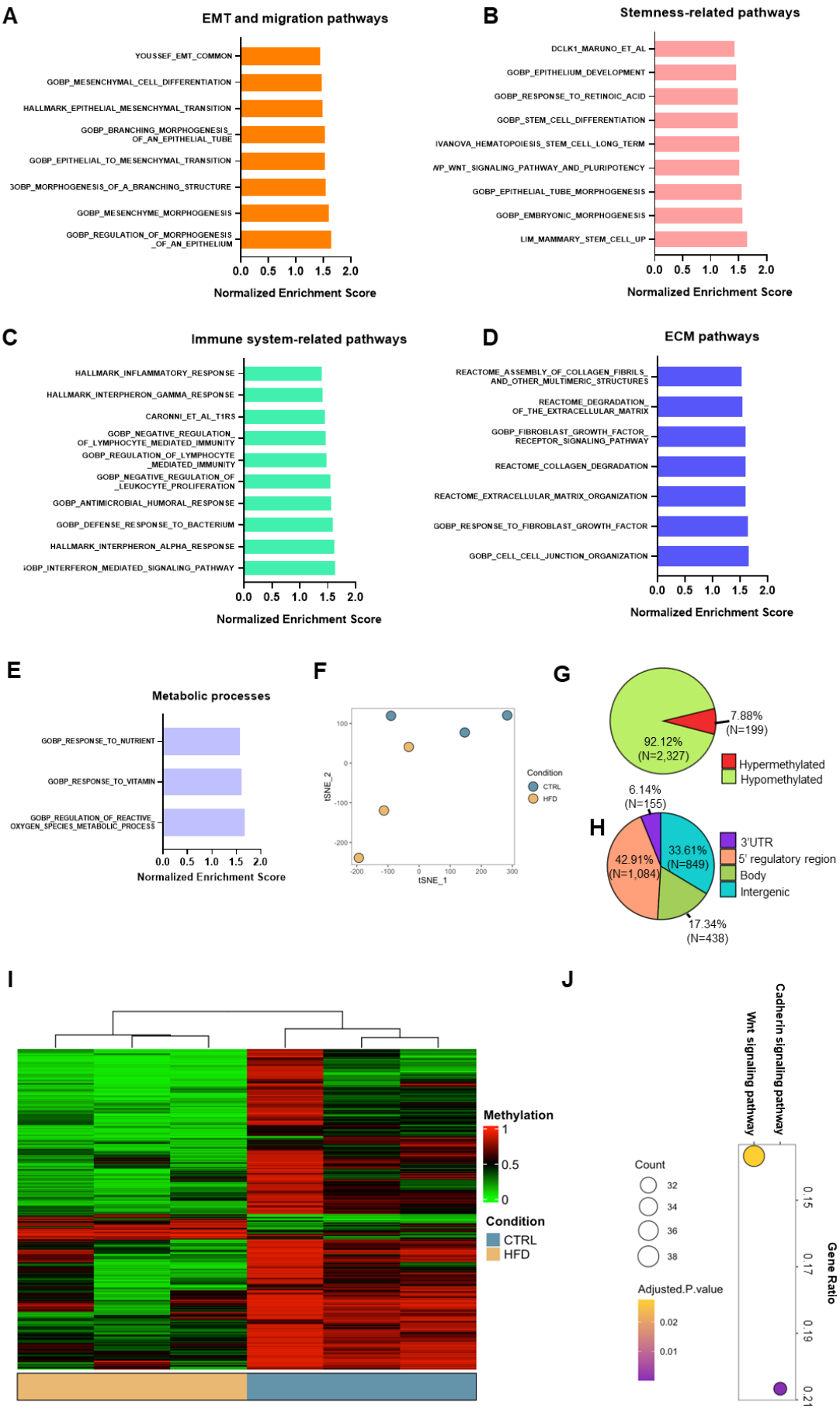
A
EMT and migration pathways
YOUSSEF_EMT_COMMON
GOBP_MESENCHYMAL_CELL_DIFFERENTIATION
HALLMARK_EPITHELIAL_MESENCHYMAL_TRANSITION
GOBP_BRANCHING_MORPHOGENESIS_OF_AN_EPITHELIAL_TUBE
GOBP_EPITHELIAL_TO_MESENCHYMAL_TRANSITION
GOBP_MORPHOGENESIS_OF_A_BRANCHING_STRUCTURE
GOBP_MESENCHYME_MORPHOGENESIS
GOBP_REGULATION_OF_MORPHOGENESIS_OF_AN_EPITHELIUM
0.0 0.5 1.0 1.5 2.0
Normalized Enrichment Score
B
Stemness-related pathways
DCLK1_MARUNO_ET_AL
GOBP_EPITHELIUM_DEVELOPMENT
GOBP_RESPONSE_TO_RETINOIC_ACID
GOBP_STEM_CELL_DIFFERENTIATION
IVANOVA_HEMATOPOIESIS_STEM_CELL_LONG_TERM
NP_WNT_SIGNALING_PATHWAY_AND_PLURIPOTENCY
GOBP_EPITHELIAL_TUBE_MORPHOGENESIS
GOBP_EMBRYONIC_MORPHOGENESIS
LIM_MAMMARY_STEM_CELL_UP
0.0 0.5 1.0 1.5 2.0
Normalized Enrichment Score
C
Immune system-related pathways
HALLMARK_INFLAMMATORY_RESPONSE
HALLMARK_INTERPHERON_GAMMA_RESPONSE
CARONNI_ET_AL_T1RS
GOBP_NEGATIVE_REGULATION_OF_LYMPHOCYTE_MEDIATED_IMMUNITY
GOBP_REGULATION_OF_LYMPHOCYTE_MEDIATED_IMMUNITY
GOBP_NEGATIVE_REGULATION_OF_LEUKOCYTE_PROLIFERATION
GOBP_ANTIMICROBIAL_HUMORAL_RESPONSE
GOBP_DEFENSE_RESPONSE_TO_BACTERIUM
HALLMARK_INTERPHERON_ALPHA_RESPONSE
GOBP_INTERFERON_MEDIATED_SIGNALING_PATHWAY
0.0 0.5 1.0 1.5 2.0
Normalized Enrichment Score
D
ECM pathways
REACTOME_ASSEMBLY_OF_COLLAGEN_FIBRILS_AND_OTHER_MULTIMERIC_STRUCTURES
REACTOME_DEGRADATION_OF_THE_EXTRACELLULAR_MATRIX
GOBP_FIBROBLAST_GROWTH_FACTOR_RECEPTOR_SIGNALING_PATHWAY
REACTOME_COLLAGEN_DEGRADATION
REACTOME_EXTRACELLULAR_MATRIX_ORGANIZATION
GOBP_RESPONSE_TO_FIBROBLAST_GROWTH_FACTOR
GOBP_CELL_CELL_JUNCTION_ORGANIZATION
0.0 0.5 1.0 1.5 2.0
Normalized Enrichment Score
E
Metabolic processes
GOBP_RESPONSE_TO_NUTRIENT
GOBP_RESPONSE_TO_VITAMIN
GOBP_REGULATION_OF_REACTIVE_OXYGEN_SPECIES_METABOLIC_PROCESS
0.0 0.5 1.0 1.5 2.0
Normalized Enrichment Score
F
tSNE_2
tSNE_1
Condition
CTRL
HFD
G
7.88% (N=199)
92.12% (N=2,327)
Hypermethylated
Hypomethylated
H
6.14% (N=155)
33.61% (N=849)
42.91% (N=1,084)
17.34% (N=438)
3'UTR
5' regulatory region
Body
Intergenic
I
Methylation
1
0.5
0
Condition
CTRL
HFD
J
Cadherin signaling pathway
Wnt signaling pathway
Gene Ratio
0.15
0.17
0.19
0.21
Count
32
34
36
38
Adjusted.P.value
0.02
0.01

1162

1163 ***Figure S2. Murine GSEA and methylation analysis. A)*** *Gene Set Enrichment Analysis (GSEA) plot showing*
1164 *the enrichment in pathways associated with EMT and migration.* ***B****) GSEA plot showing the enrichment in*
1165 *pathways associated with stemness.* ***C)*** *GSEA plot showing the enrichment in pathways associated with the*
1166 *immune system and inflammatory processes.* ***D)*** *GSEA plot showing the enrichment in pathways associated*
1167 *with extracellular matrix (ECM).* ***E)*** *GSEA plot showing the enrichment in pathways associated with metabolic*
1168 *processes.* ***A-B-C-D-E)*** *FDR<0.25.* ***F)*** *t-SNE representing unsupervised analysis of control (CTRL) and high-*
1169 *fat diet (HFD) primary tumor cell lines for methylation assessment.* ***G-H)*** *Pie charts showing the number of*
1170 *differentially hyper and hypomethylated CpG sites between control and HFD cell lines (top panel) and the*
1171 *location of the sites (bottom panel).* ***I)*** *Heatmap showing the clustering of CTRL and HFD cell lines based on*
1172 *the differentially methylated CpG sites.* ***J)*** *Enrichment plot showing the pathways differentially methylated for*
1173 *HFD versus CTRL cell lines.*

1174

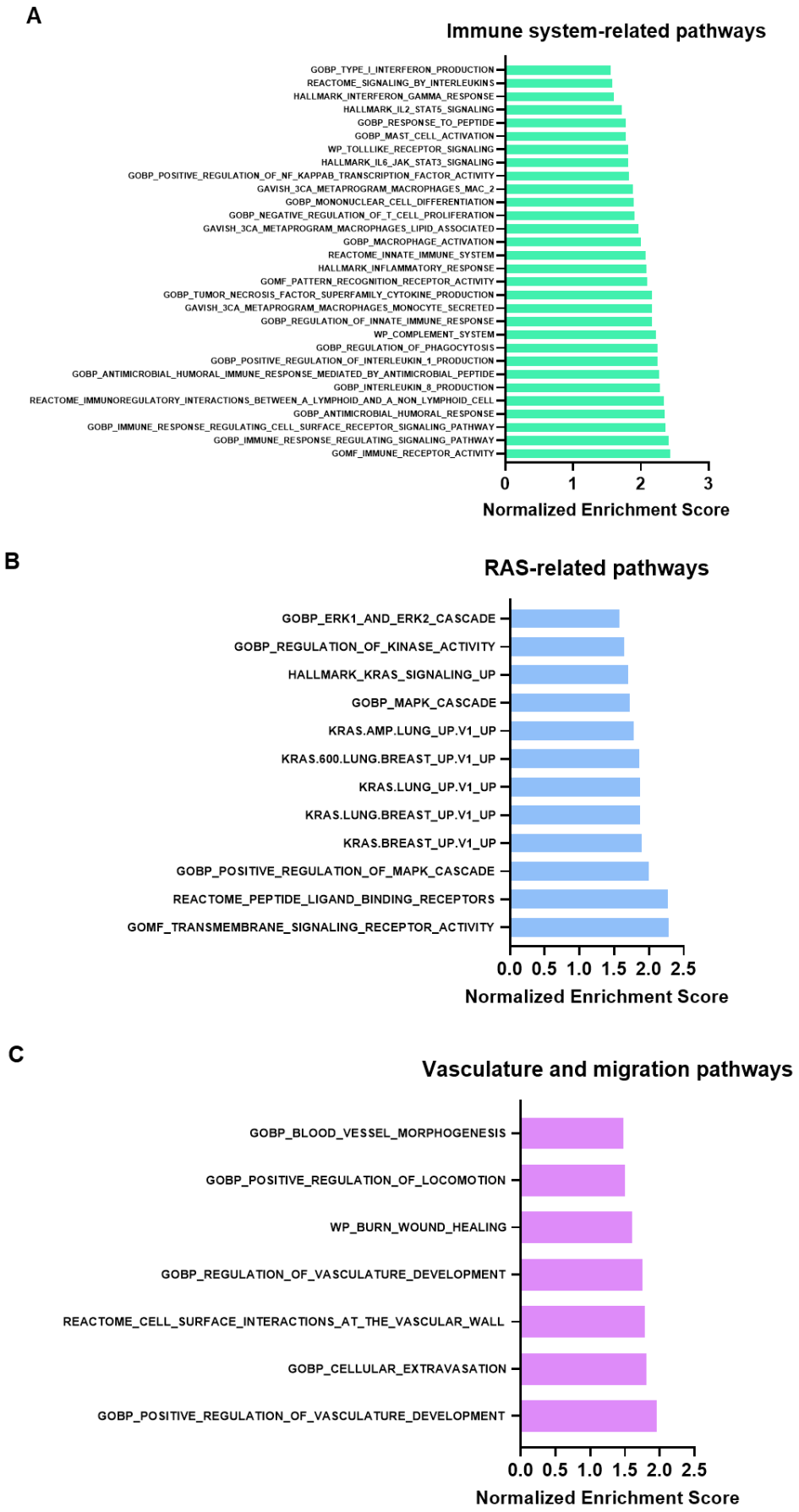
A
Immune system-related pathways
GOBP_TYPE_I_INTERFERON_PRODUCTION
REACTOME_SIGNALING_BY_INTERLEUKINS
HALLMARK_INTERFERON_GAMMA_RESPONSE
HALLMARK_IL2_STAT5_SIGNALING
GOBP_RESPONSE_TO_PEPTIDE
GOBP_MAST_CELL_ACTIVATION
WP_TOLLLIKE_RECEPTOR_SIGNALING
HALLMARK_IL6_JAK_STAT3_SIGNALING
GOBP_POSITIVE_REGULATION_OF_NF_KAPPAB_TRANSCRIPTION_FACTOR_ACTIVITY
GAVISH_3CA_METAPROGRAM_MACROPHAGES_MAC_2
GOBP_MONONUCLEAR_CELL_DIFFERENTIATION
GOBP_NEGATIVE_REGULATION_OF_T_CELL_PROLIFERATION
GAVISH_3CA_METAPROGRAM_MACROPHAGES_LIPID_ASSOCIATED
GOBP_MACROPHAGE_ACTIVATION
REACTOME_INNATE_IMMUNE_SYSTEM
HALLMARK_INFLAMMATORY_RESPONSE
GOMF_PATTERN_RECOGNITION_RECEPTOR_ACTIVITY
GOBP_TUMOR_NECROSIS_FACTOR_SUPERFAMILY_CYTOKINE_PRODUCTION
GAVISH_3CA_METAPROGRAM_MACROPHAGES_MONOCYTE_SECRETED
GOBP_REGULATION_OF_INNATE_IMMUNE_RESPONSE
WP_COMPLEMENT_SYSTEM
GOBP_REGULATION_OF_PHAGOCYTOSIS
GOBP_POSITIVE_REGULATION_OF_INTERLEUKIN_1_PRODUCTION
GOBP_ANTIMICROBIAL_HUMORAL_IMMUNE_RESPONSE_MEDIATED_BY_ANTIMICROBIAL_PEPTIDE
GOBP_INTERLEUKIN_8_PRODUCTION
REACTOME_IMMUNOREGULATORY_INTERACTIONS_BETWEEN_A_LYMPHOID_AND_A_NON_LYMPHOID_CELL
GOBP_ANTIMICROBIAL_HUMORAL_RESPONSE
GOBP_IMMUNE_RESPONSE_REGULATING_CELL_SURFACE_RECEPTOR_SIGNALING_PATHWAY
GOBP_IMMUNE_RESPONSE_REGULATING_SIGNALING_PATHWAY
GOMF_IMMUNE_RECEPTOR_ACTIVITY
0
1
2
3
Normalized Enrichment Score
B
RAS-related pathways
GOBP_ERK1_AND_ERK2_CASCADE
GOBP_REGULATION_OF_KINASE_ACTIVITY
HALLMARK_KRAS_SIGNALING_UP
GOBP_MAPK_CASCADE
KRAS.AMP.LUNG_UP.V1_UP
KRAS.600.LUNG.BREAST_UP.V1_UP
KRAS.LUNG_UP.V1_UP
KRAS.LUNG.BREAST_UP.V1_UP
KRAS.BREAST_UP.V1_UP
GOBP_POSITIVE_REGULATION_OF_MAPK_CASCADE
REACTOME_PEPTIDE_LIGAND_BINDING_RECEPTORS
GOMF_TRANSMEMBRANE_SIGNALING_RECEPTOR_ACTIVITY
0.0
0.5
1.0
1.5
2.0
2.5
Normalized Enrichment Score
C
Vasculature and migration pathways
GOBP_BLOOD_VESSEL_MORPHOGENESIS
GOBP_POSITIVE_REGULATION_OF_LOCOMOTION
WP_BURN_WOUND_HEALING
GOBP_REGULATION_OF_VASCULATURE_DEVELOPMENT
REACTOME_CELL_SURFACE_INTERACTIONS_AT_THE_VASCULAR_WALL
GOBP_CELLULAR_EXTRAVASATION
GOBP_POSITIVE_REGULATION_OF_VASCULATURE_DEVELOPMENT
0.0
0.5
1.0
1.5
2.0
2.5
Normalized Enrichment Score

1175

1176 ***Figure S3. GSEA from human samples. A)*** *Gene Set Enrichment Analysis (GSEA) plot showing the*
1177 *enrichment in pathways associated with the immune system and inflammatory processes.* ***B)*** *GSEA plot*
1178 *showing the enrichment in pathways associated with RAS-related pathways.* ***C)*** *GSEA plot showing the*
1179 *enrichment in pathways associated with vasculature and migration. FDR<0.25.*

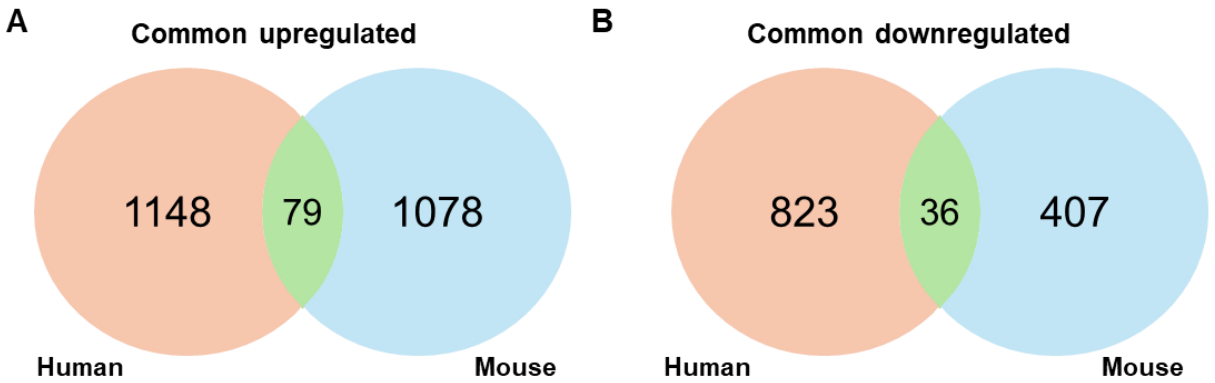

1180

1181

1182 ***Figure S4. Venn Diagrams of common up and downregulated genes in human and murine datasets. A-***
1183 ***B)*** *Venn diagrams showing the number of genes commonly upregulated (A) or downregulated (B) found in our*
1184 *murine and human databases.*

1185

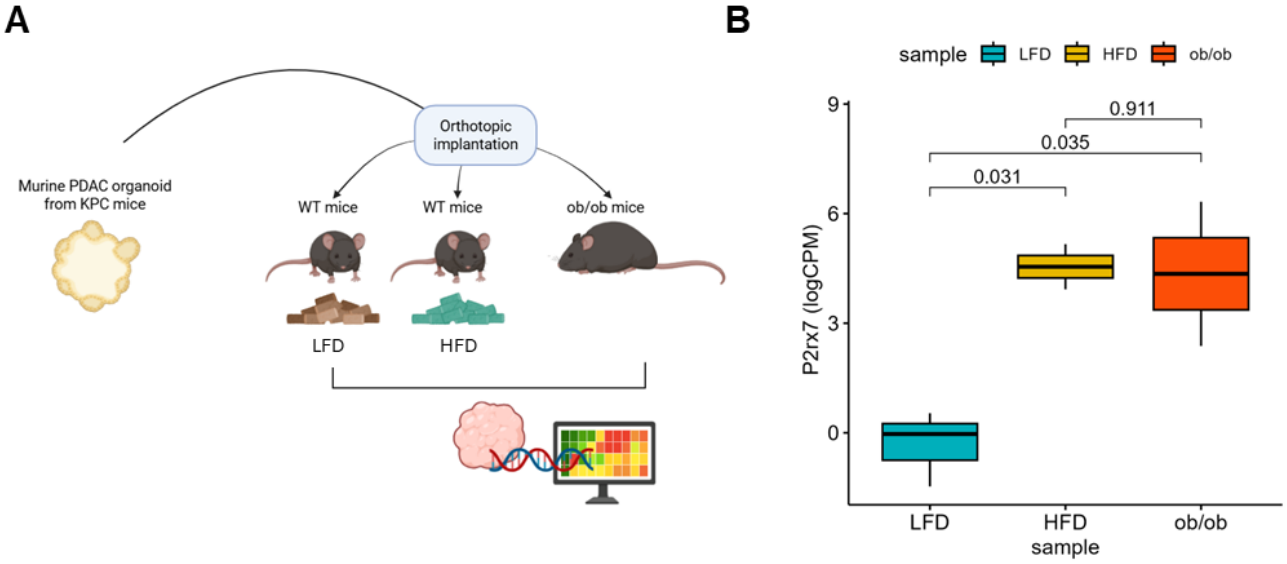

1186

1187 ***Figure S5. Tumor-derived organoids grown in high-fat diet-fed and ob/ob mice recapitulate P2RX7***
1188 ***overexpression. A)*** *Schematic representation of the experimental setting to study how murine tumor-derived*
1189 *organoids generate tumors in three different hosts (C57Bl/6 mice fed with control or low fat (LFD) diet, HFD or*
1190 *ob/ob mice).* ***B)*** *Box plots showing the levels of P2rx7 expression by RNA-seq in tumors generated in the three*
1191 *different hosts, showing the mean ± STDEV of logCPM (n for LFD=3, n for HFD=2, n for ob7ob=2 P values as*
1192 *determined by Dunn test).*

1193

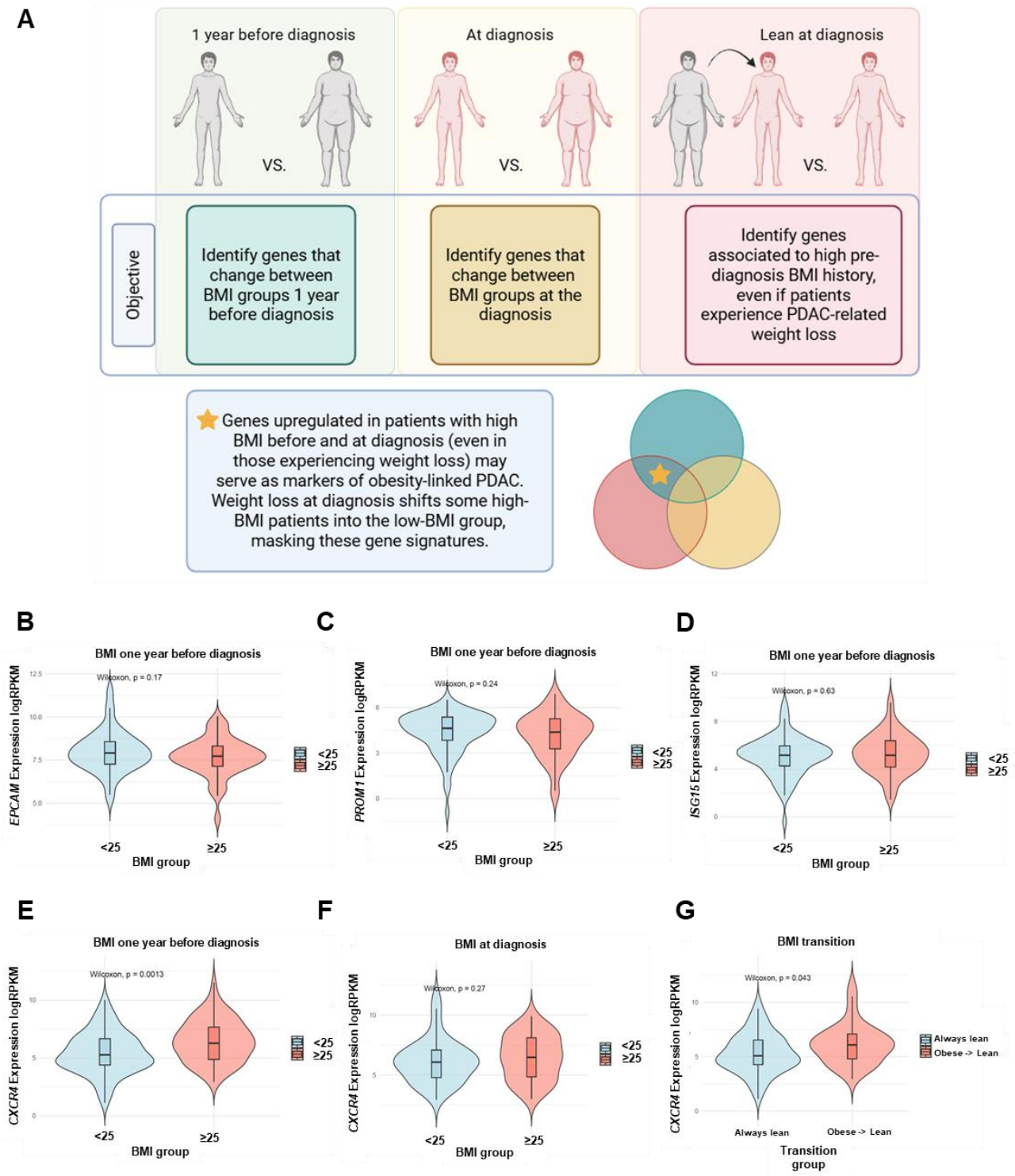

Figure S6. Description of the comparisons in our patient cohort and evaluation of stem markers in patients with high and low BMI. A) *Diagram showing the comparisons employed to study the transcription diferences between patients with high BMI (BMI≥25) or low BMI (BMI<25) at different timepoints.* ***B)*** *Violin plot showing the quantification of EPCAM expression in PDAC patients based on their BMI 1 year before diagnosis.* ***C)*** *Violin plot showing the quantification of PROM1 expression in PDAC patients based on their BMI 1 year before diagnosis.* ***D)*** *Violin plot showing the quantification of ISG15 expression in PDAC patients based on their BMI 1 year before diagnosis.* ***E)*** *Violin plot showing the quantification of CXCR4 expression in PDAC patients based on their BMI 1 year before diagnosis.* ***F)*** *Violin plot showing the quantification of CXCR4 expression in PDAC patients based on their BMI at time of diagnosis.* ***G)*** *Violin plot showing the quantification of CXCR4*

expression in PDAC patients based on their BMI transition (patients previously obese that lost their weight versus those that always present a BMI<25). P values as determined by Wilcoxon test.

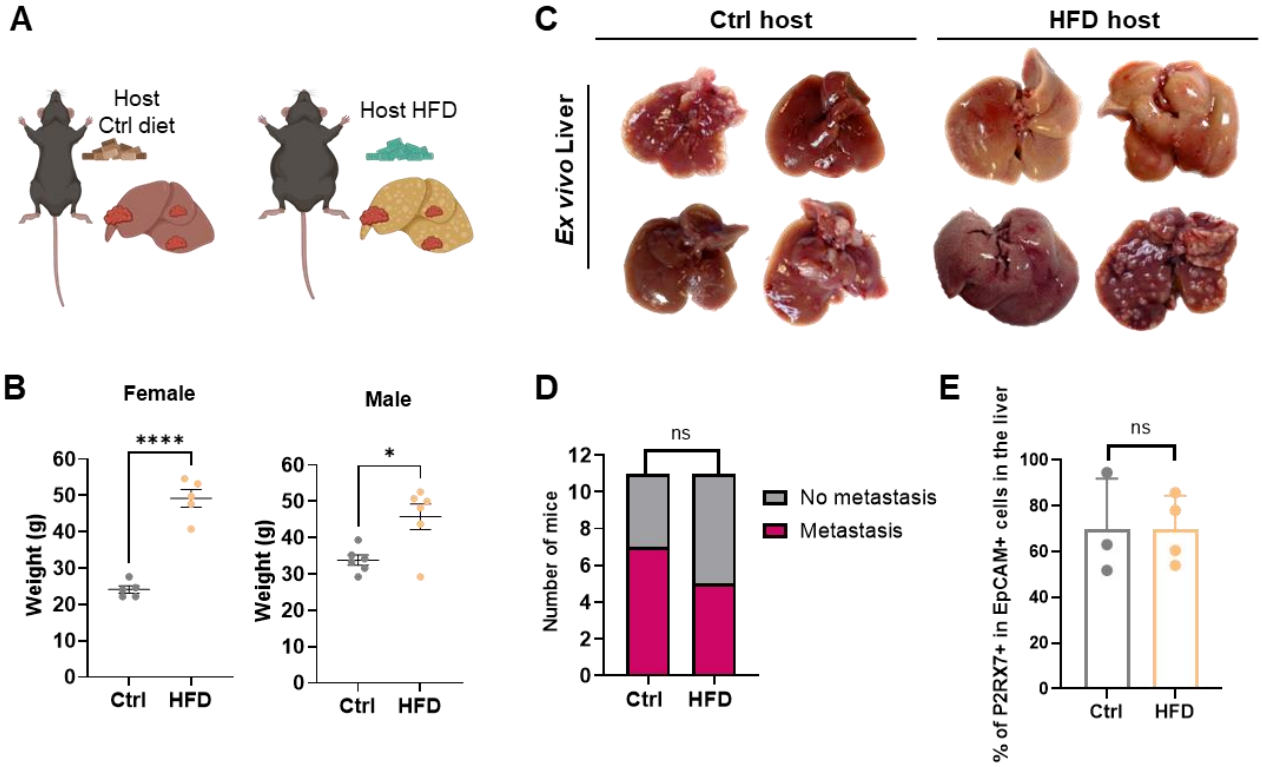

Figure S7. Host-dependent metastatic capacity of control cells. A) *Diagram showing the two kinds of hosts employed for the intrasplenic assay with control (Ctrl) cell lines.* ***B)*** *Evaluation of body weight in female and male mice included in the study prior to the experiment. Shown is the mean ± SEM, P values as determined by unpaired T-test).* ***C)*** *Representative images of ex vivo livers from control and high-fat diet (HFD) mice with different degrees of macrometastatic disease.* ***D)*** *Number of mice presenting metastatic disease or not visible metastasis in the lean/control and HFD groups (n=11, P values as determined by Chi-square and Fisher´s exact test).* ***E)*** *Quantification of the percentage of P2RX7 positive cells in the detected EpCAM positive events in control and HFD livers from this experiment. Shown is the mean ± STDEV (n=3 mice, P values as determined by unpaired T-test). P values: *, <0.05; **, <0.01; ***, <0.001; ****, <0.0001.*

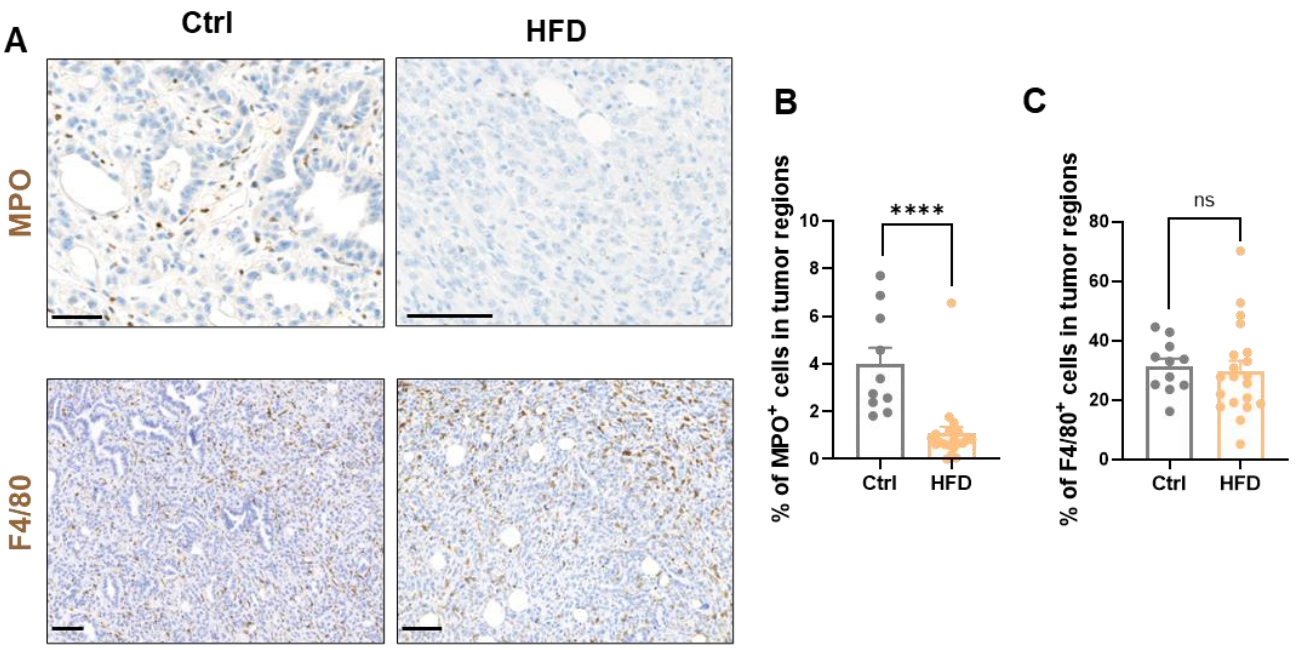

Figure S8. Neutrophil and macrophage infiltration in HFD tumors. A) *Representative brightfield images of Ctrl and HFD mice tumors stained with anti-MPO (neutrophils) (scale bar = 50 µm on the left image and 100 µm on the right) or anti-F4/80 (macrophages) (scale bar = 100 µm) by immunohistochemistry.* ***B-C)*** *Quantification of MPO and F4/80 positive cells in pancreatic tumor regions in Ctrl and HFD mice. Shown is the mean ± SEM (n=3 mice for Ctrl group and 5 mice for HFD group, each dot represents a tumor region, P values as determined by unpaired T-test). P values: *, <0.05; **, <0.01; ***, <0.001; ****, <0.0001.*

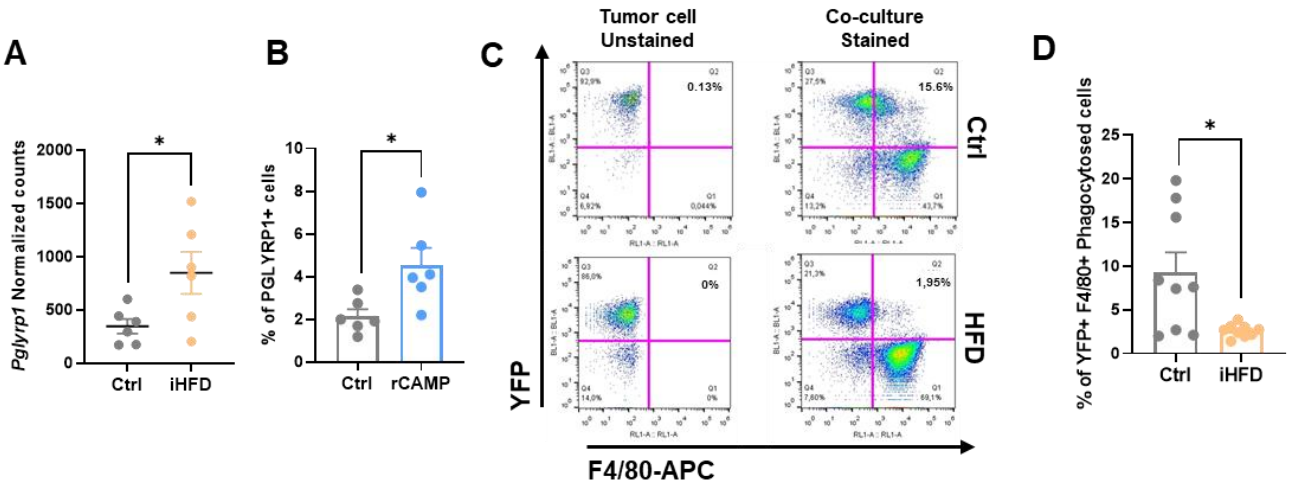

Figure S9. CAMP induces P2RX7 and PGLYRP1 protecting tumor cells from macrophage phagocytosis. A) *Quantification of Pglyrp1 expression in control (Ctrl) and high-fat diet (HFD) primary murine cell lines included in the RNA-seq analyses. Shown is the mean ± SEM (n=6, P values as determined by T-test).* ***B)*** *Quantification of PGLYRP1 positive cells treated with recombinant (r) CAMP (100 µg/mL) for 48 hours. Shown is the mean ± SEM (n=6, P values as determined by unpaired T-test).* ***C)*** *Representative flow cytometry plots showing YFP positive control (Ctrl) and high-fat diet (HFD) primary tumor cells co-cultured with primary bone marrow-derived macrophages stained with F4/80. Live double positive events count as phagocytosed cells.* ***D)*** *Quantification of the percentage of phagocytosed tumor cells by flow cytometry. Shown is the mean ± SEM (n=3 cell lines in triplicates, P values as determined by unpaired T-test). P values: *, <0.05; **, <0.01; ***, <0.001; ****, <0.0001.*

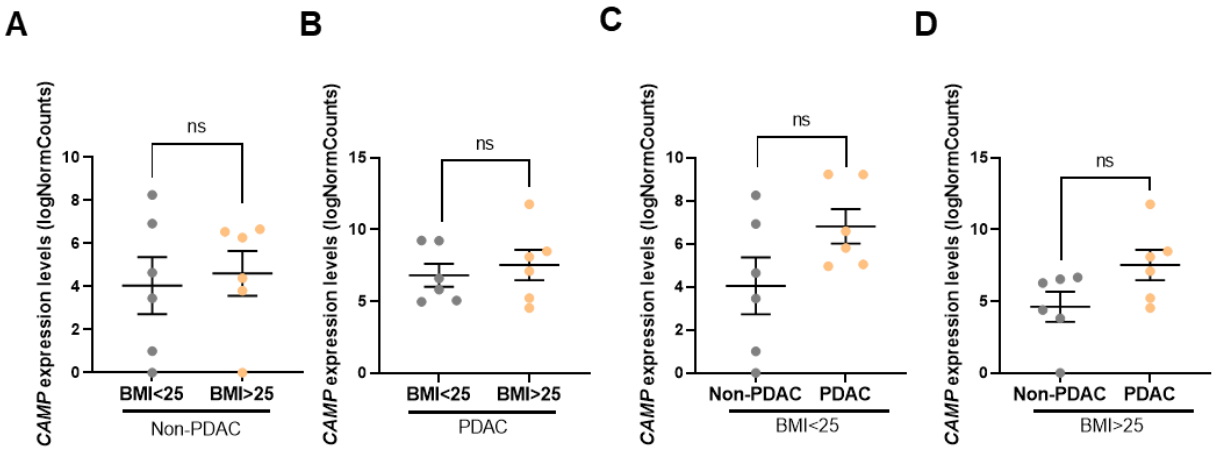

Figure S10. CAMP can be detected in PBMCs from patients although it is not differentially expressed in circulation. A-B) *Quantification of CAMP expression levels in PBMCs from non-PDAC (A) and PDAC patients (B) with BMI higher or lower than 25. Shown is the mean ± SEM (n=6 patients per group, P values as determined by unpaired T-test).* ***C-D)*** *Quantification of CAMP expression levels in PBMCs from low BMI (C) and high BMI patients (D) either with non-PDAC or PDAC. Shown is the mean ± SEM (n=6 patients per group, P values as determined by unpaired T-test). P values: *, <0.05; **, <0.01; ***, <0.001; ****, <0.0001.*

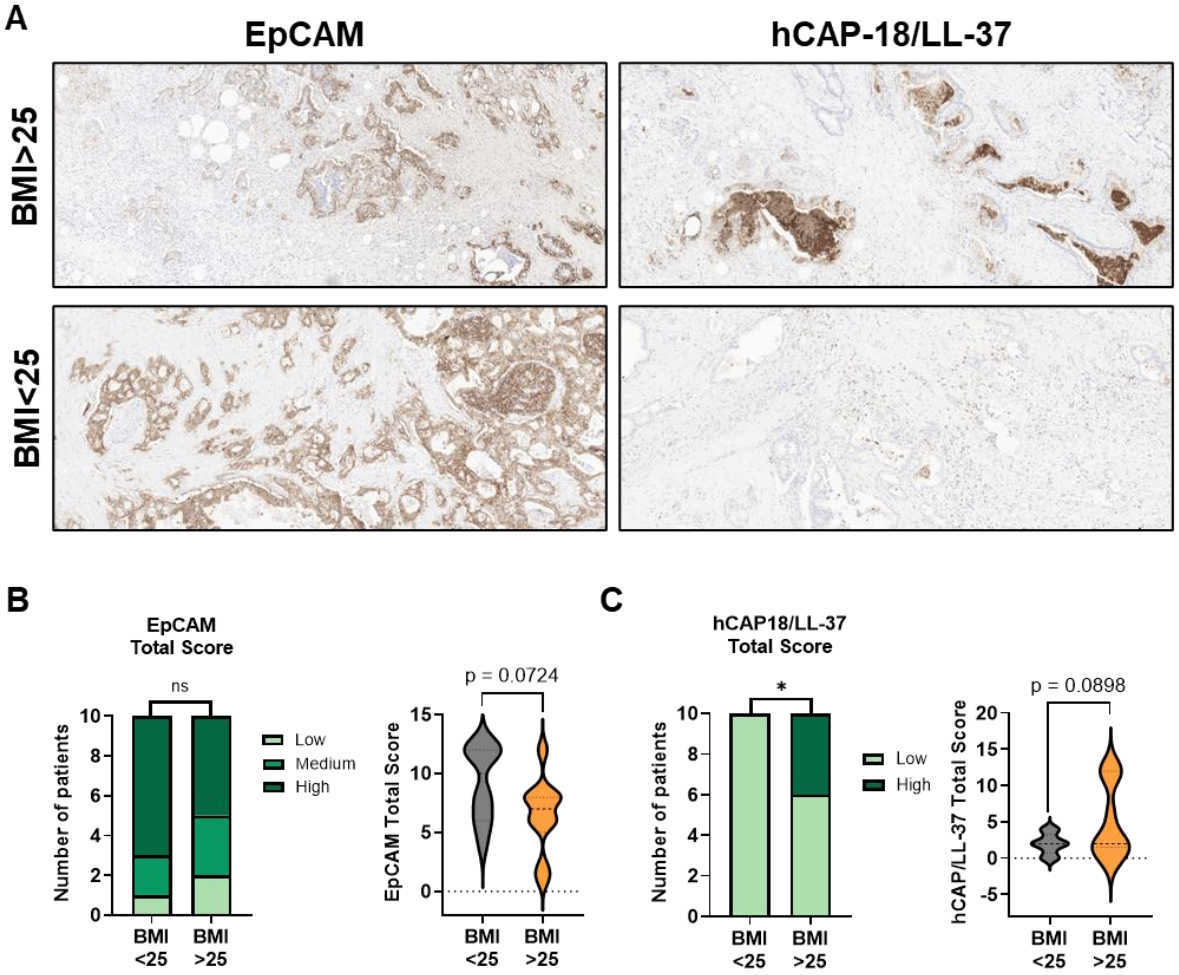

Figure S11. Patients with higher BMI present lower EpCAM and higher hCAP-18/LL-37 intratumoral levels. A) *Representative brightfield images of PDAC tumors from patients with BMI>25 or BMI<25 stained with anti-EpCAM (epithelial tumor cells) or anti-hCAP-18/LL-37 by immunohistochemistry. Magnification for all images was 20x.* ***B)*** *Quantification of patient's proportion presenting high, medium or low EpCAM levels of the above mentioned stainings (left panel) and the EpCAM total score of all samples (right panel). Shown is the total score (% of staining x intensity), P values as determined by Chi-square and Fisher´s exact test (left panel) and unpaired T-test (right panel).* ***C)*** *Quantification of patient's proportion presenting high, medium or low hCAP-18/LL-37 levels of the above mentioned stainings (left panel) and the hCAP-18/LL-37 total score of all samples (right panel). Shown is the total score (% of staining x intensity), P values as determined by Chi-square and Fisher´s exact test (left panel) and unpaired T-test (right panel). P values: *, <0.05; **, <0.01; ***, <0.001; ****, <0.0001.*